

Manuscript version: Author's Accepted Manuscript

The version presented in WRAP is the author's accepted manuscript and may differ from the published version or Version of Record.

Persistent WRAP URL:

<http://wrap.warwick.ac.uk/166486>

How to cite:

Please refer to published version for the most recent bibliographic citation information. If a published version is known of, the repository item page linked to above, will contain details on accessing it.

Copyright and reuse:

The Warwick Research Archive Portal (WRAP) makes this work by researchers of the University of Warwick available open access under the following conditions.

© 2022 Elsevier. Licensed under the Creative Commons Attribution-NonCommercial-NoDerivatives 4.0 International <http://creativecommons.org/licenses/by-nc-nd/4.0/>.



Publisher's statement:

Please refer to the repository item page, publisher's statement section, for further information.

For more information, please contact the WRAP Team at: wrap@warwick.ac.uk.

Numerical and random forest modelling of the impact response of hierarchical auxetic structures

Ahmed Haytham Tajalsir Ahmed^a, K.B. Mustapha^{1a}, T. Ibn-Mohammed^b

^aDepartment of Mechanical, Materials and Manufacturing Engineering, University of Nottingham (Malaysia Campus), 43500 Semenyih, Malaysia

^bWarwick Manufacturing Group (WMG), The University of Warwick, Coventry CV4 7AL, United Kingdom

Abstract

Major sources of concern when auxetic protective structures are deployed in service of mission-critical applications encompass the triggering of high impact stress and the weakening of the structures' elastic strength in response to the impact events. The current prevailing approach to assessing the impact resistance of these structures broadly hinges on mechanics-informed nonlinear finite element (FE) analysis. However, this method is computationally expensive and ill-suited for tackling the implementation of automated condition monitoring schemes. To address the above issues, first, this paper proposes a hybrid hierarchical auxetic structure named Hybrid-Hierarchical Re-entrant Honeycomb (HHRH) that is endowed with a feature that dialed down the impact stress. Next, using explicit FE, the investigation proceeds to uncover the interplay between the key geometric features of this HHRH auxetic structure and the impact performance under low, intermediate, and high crushing velocities. The focus then steered towards unifying the outcome of the nonlinear explicit FE simulations with random forests (RF) scheme towards the establishment of intelligent auxetic structural systems. The results revealed that the developed HHRH maintained the auxeticity of the regular re-entrant auxetic and exhibited superior performance in some crushing strain regions. Moreover, the HHRH structure manifests up to an 85% reduction in peak stress and the proposed reinforcement boosts the auxetic property by up to 23% when compared to the regular re-entrant auxetic structure under high-velocity applications. As for the established data-driven RF-enabled machine learning model, its predictive strength with optimally-tuned hyperparameters is demonstrated to excellently capture the nonlinear multi-modal crushing stress response at various crushing strains, velocities, and geometric variations.

Keywords:

Re-entrant auxetics; Hierarchical auxetics; Lightweight structures; Impact analysis; Finite Element Analysis; Random Forest modelling

¹Corresponding author. Telephone: +60387253482, E-mail: KhameelB.Mustapha@nottingham.edu.my (K.B. Mustapha)

1. Introduction

The present work relates to the performance assessment of auxetic structures. Category-wise, auxetic structures reside within a cluster of materials known as cellular structural systems. A comprehensive account of the behaviour of cellular materials is documented by Gibson and Ashby [1]. Often inspired by nature, man-made cellular materials have emerged as excellent candidates in the quest to concurrently reduce the weight and carbon footprint of structural systems without sacrificing stiffness and strength [2, 3]. One notable feature of the general cellular materials is the close link between their mechano-physical responses and the architecture of their unit cells [4]. In the specific case of auxetic materials, an additional distinguishing feature emerged in the form of negative Poisson's ratio (NPR). The implication of NPR is counterintuitive. It dictates that when an auxetic material is stretched axially, lateral expansion occurs (as opposed to shrinking as is common in conventional materials). Crucially, this NPR effect translates to the enhancement of shear modulus, which has led to the emergence of difficult-to-shear, but volumetrically easy-to-deform structures [5]. Other distinct effects of NPR include elevated indentation resistance, enhanced fracture toughness, boosted energy absorption property/crash resistance, and synclastic curvature, among others [6-10]. Historically, the very concept of materials with negative or zero Poisson's ratio is traced to the work of Love [11], as chronicled by Prawoto [12]. Around the late 1980s, Lakes [13, 14] pioneered the synthesis of isotropic auxetic foams. This breakthrough accelerated the development of what has now become an important class of structural materials. Since Lake's landmark study, scholars have pursued investigations into the theoretical analytical/numerical modelling [15-20], manufacturing [21] and performance assessments of auxetic material systems as highlighted in some of the recent review papers [7, 22-25].

From a static analysis perspective, factors that influence the mechanical response of various auxetic structures have been comprehensively studied. A notably non-thorough list of selected studies along this line is given next. Choi and Lakes [26] investigated the linear elastic response of re-entrant foams. The study upheld the link between the static mechanical response of general auxetics to change in the shape of the internal structure from convex to concave. Lee, et al. [27] applied a homogenization finite element analysis to assess the linear elastic response of re-entrant auxetics. Wan, et al. [28] reported the application of large deflection beam theory to the static simulation of soft polymeric re-entrant auxetics structures. It was shown that the Poisson's ratios of auxetic materials vary significantly with strain under large deformation loading scenarios. The effects of cell wall size and cell wall angle on the static performance of re-entrant auxetics are covered in the study by Yang, et al. [17], Gonella and Ruzzene [19], Rad, et al. [29], and Fu, et al. [30], among others. Beyond the above studies based on the response of defect-free auxetic structures, some authors have spearheaded investigations into the influence of imperfections on the behaviour of auxetics. For instance, Liu, et al. [31] studied the effect of manufacturing-induced irregularity on the effective mechanical properties of re-entrant honeycomb auxetics. Recently, Gao, et al. [32] presented a four-step analytical framework to investigate the effects of irregularity on the elastic properties of double arrowed auxetics. It was reported that the effective Young's modulus of the auxetic is more sensitive to the presence of imperfections than the Poisson's ratio. Parallel to the aforementioned studies, important investigations have also been devoted to the assessments of the performance of

various types of auxetics under dynamic loading scenarios [33]. This is understandable considering the usages of auxetic structures for impact and shock absorption applications (such as damper and body armour, etc.). One of the earliest studies on the crushing resistance of auxetic structures is reported by Scarpa, et al. [34]. The results indicate an overall superiority displayed by the auxetic structures in damping and acoustic properties compared to conventional foams. Henderson, et al. [35] compared the effect of defects on the crush performance of auxetic and non-auxetic honeycombs. It was highlighted that the reduction of the crush performance in the auxetic honeycomb is less severe. Zhang, et al. [36] investigated the in-plane dynamic crushing behaviour of re-entrant honeycombs within a certain range of cell-wall properties. The study showed that an increase in the thickness of the unit cell enhances the plateau stress. Besides, it was demonstrated that changes in the cell-wall angle create different collapse modes, while the magnitude of the impacting velocity creates different localization bands. The effects of cell wall angle, cell-wall length ratio and variation of impact velocity on the dynamic response were studied by Hu, et al. [37]. Gao, et al. [38] studied the deformation patterns of double arrowed honeycomb auxetics under low/high impact velocities and presented analytical models for the dynamic strength based on the idea of cellular collapse mechanism. The authors concluded that the crushing strengths of the double arrowed honeycomb auxetic structure rise with the increase of relative density. The response of auxetic composite structures under blast loading is reported in [39-41].

Collectively, the above studies have dealt with a variety of 2D and 3D auxetic structures ranging in size (molecular, microscale to macroscale) and shape (re-entrant, chiral, anti-chiral, rotating unit type auxetic structures etc.) [42, 43]. Nevertheless, towards the deployment of auxetic structures in the mitigation of dynamic impact damages, it has been established that many categories of lightweight materials (such as auxetics, cellular materials, thin-walled foam-filled tubes, etc) suffer from low stiffness [44, 45]. A detrimental consequence of low stiffness is the acceleration of failure by yielding, which may arise from high internal stress when these auxetic structures are exposed to extreme impacting events [46]. For instance, according to Baran and Öztürk [47], re-entrant auxetics have limited applications as a result of the low rigidity of the unit cell. For the above reasons, a growing body of research has emerged with a focus on improving the stiffness of many classical auxetic structures. The challenge though is that improving the stiffness may often lead to the loss of the auxetic behaviour [44]. Nonetheless, certain strategies have been proposed to retain the NPR effect, improve the stiffness, and enhance the crushing performance of various types of auxetic structures. Along this line, Zied, et al. [48] presented an improvement to the in-plane stiffness of hexagonal re-entrant auxetics through the modification of the basic structure with spline edges and stiffener. In a similar vein, Ingrole, et al. [49] proposed a set of new designs for re-entrant honeycomb structure to provide enhanced in-plane stiffness properties. Novak, et al. [50] considered the use of graded materials to tailor the mechanical behaviour of auxetic structures derived from inverted tetrapods. Gao and Liao [51] proposed the combination of gradient arrowhead auxetics with thin-walled tubes and investigated its crashworthiness performance using the finite element method. More recently, Wu, et al. [52] investigated the use of cell-wall angle gradation in a study on a planar auxetic structure with re-entrant unit cells. Li, et al. [53] modified the re-entrant unit cell topology by adding a vertical beam element, leading to increased Young's modulus and yield strength.

Compared to the above methods of enhancing the properties of auxetics, the use of hierarchy and a rigorous investigation of the mechanical behaviour of the ensuing hierarchical auxetic structures remains fully unexplored. Indeed, the crushing response of hierarchical auxetic structures under high impact velocities has not been fully tackled in literature, although it was widely used for strengthening traditional honeycomb structures [54]. Among the very few studies on the use of hierarchical architecture in the context of auxetics, Zhang, et al. [55] considered the in-plane mechanical behaviour of the hierarchical star-re-entrant metamaterial. Tan, et al. [56] investigated the re-entrant hierarchical honeycombs constructed by replacing the cell walls of re-entrant honeycombs with a regular hexagon substructure. These studies not only showed lower plateau stresses for the first and second-order hierarchical structures, but they also revealed that the hierarchical auxetic structures exhibited very high energy absorption capacity. In practice, a limiting barrier to the wider applications of hierarchical structures is manufacturing. Therefore, given the possible difficulty in the manufacturing of hierarchical auxetics proposed in the existing studies, the current study investigates a new hierarchical auxetic. Specifically, the current work bears similarities to that of Hou, et al. [57]. The similarity stems from the restriction of the hierarchical elements to the vertex rather than the cell walls. This approach limits the number of hierarchical elements and facilitates a faster fabrication procedure while enhancing the mechanical properties of the base auxetic structure. However, in contrast with [57], the current study mobilizes a series of micro-scale hexagonal structures to reinforce a typical re-entrant. Consequently, this paper investigates the response of these new hierarchical auxetics under low, intermediate, and high impacting velocities via nonlinear dynamic finite element analyses (FEA). In addition to this, the paper incorporates the development of a new data-driven predictive methodology for unravelling the crushing response of the auxetics after impact. To the best of our knowledge, this sets the work apart from all previous studies where the analysis of auxetics has been approached majorly from the numerical solution perspective. The primary motivation that drives this approach rests on the deployment of auxetics in defence-facing and aerospace applications. These use cases often raise the risk of damage from impact events that may consequently hamstring the true value of these materials [58]. Typically, the characterization of impact depends on the estimation of location and magnitude of the impact via streams of data collected through embedded sensors. For this reason, the reconstruction of the impact location and magnitude becomes an inverse problem that requires a series of expensive experiments [59]. However, of late, a cost-effective method that has become accepted is to funnel the data obtained from the solution of the forward problem enabled by nonlinear FEA into the machine learning pipeline. Using this approach, several scholars have developed expert systems for the structural health monitoring of composite structures [60]. For this study, we introduce the capability of the random forest (RF) scheme, an excellent algorithm for regression and classification tasks [47]. Consequently, the work comprises two contributions that modestly address the design of impact-tolerant auxetics and the establishment of a machine learning-enabled framework for condition monitoring/impact detection of intelligent auxetic structural systems.

The rest of the presentation is as follows. Section 2 introduces the methodology. The results from analyses with the nonlinear dynamic finite element analyses and random forest models are discussed in section 3, while section 4 covers the conclusions from the study.

2. Materials and Methods

2.1 Geometric modelling of the auxetic structure

A hierarchical auxetic structure named Hybrid-Hierarchical Re-entrant Honeycomb (HHRH) is developed by reinforcing the vertices of the conventional re-entrant auxetic unit cell with scaled hexagonal unit cells. As highlighted in the introduction, an unfavourable consequence of low stiffness in conventional re-entrant auxetics is the acceleration of failure by yielding which may originate from high internal stress when exposed to extreme impacting events [46]. Thus, a primary motivation for this new design is to enhance the stiffness, without sacrificing the NPR effect, of the re-entrant auxetic unit cell. Schematics of the hierarchical unit cell are depicted in Figure 1(a), while Figure 1(b) indicates the integrated area of the unit cell (explained further in section 2.2). Meanwhile, Figure 1(b) describes the key geometric features of the HHRH unit cell. That is: h (the length of the horizontal edge); l (the length of the slanted edge); t (the thickness of the edge), and θ (the re-entrant angle).

In this study, θ is kept constant at a value of 60° for the HHRH. However, h and l are altered in response to changes in the scaling parameter (γ) while maintaining the overall horizontal and slanted lengths of the parent re-entrant unit cell at values of 10 mm and 5 mm respectively as shown in Figure 1.

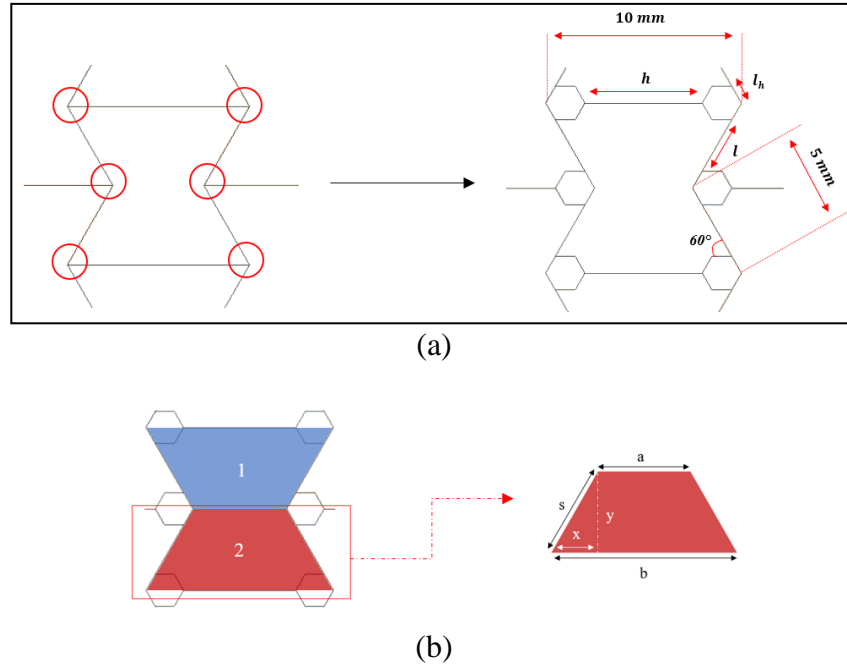


Figure 1: (a) Modification of a conventional re-entrant unit cell (zero-order) to a first-order hierarchical unit cell; (b) the integrated areas of the unit cell.

Based on the above-specified transformation, the scaling parameter γ is derived as the ratio of the hexagon edge length to the horizontal length of the unit cell ($l_h/10$). Consequently,

three different models $\gamma = 0.05, 0.1$ and 0.15 were developed with varying hexagon sizes as shown in Figure 2.

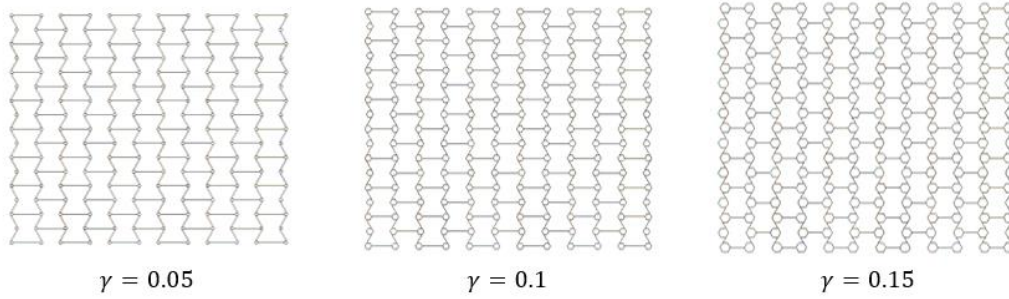


Figure 2: Variation of the hierarchical models based on the unit cell

The performance of the three models is later compared with the conventional re-entrant hexagonal structure which has a γ value of 0. Table 1 summarizes the geometric values used in all models. It will be noticed that different thickness values are used for each model to maintain a constant relative density.

Table 1: Values of the geometric variables

γ	l (mm)	h (mm)	l_h (mm)	t (mm)
0	5	10	0	0.62
0.05	4	8	0.5	0.42
0.10	3	6	1	0.30
0.15	2	4	1.5	0.19

2.2 Basic theoretical analysis

The mechanical properties of cellular materials depend on the relative density, $\Delta\rho$ [1]. As a result, maintaining a constant relative density will ensure a fair comparison of performance between the models. Meanwhile, the relative densities of the classical re-entrant, $\Delta\rho_r$, and that of the hexagon, $\Delta\rho_h$, cellular structures are given as [61]:

$$\Delta\rho_h = \frac{2t}{\sqrt{3}l} \quad (1)$$

$$\Delta\rho_r = \frac{1}{2} \frac{t}{l} \frac{h/l+2}{\cos \alpha(h/l+\sin \alpha)} \quad (2)$$

where α is $90 - \theta$. Based on the equations above, a modified expression for the newly established HHRH is formulated by integrating the area fractions of the hexagon and re-entrant elements in the structure as:

$$\Delta\rho = A_h \Delta\rho_h + (1 - A_h) \Delta\rho_r \quad (3)$$

where A_h is the area fraction of the hexagonal element. To find A_h , it is noted that the total area of the hierarchical unit cell is the additive sum of two trapezoidal areas and 4 full hexagonal areas (as indicated in Figure 1(b)). The areas of a trapezoid (A_t) and that of a regular hexagon (A_{hex}) are defined as:

$$A_t = \frac{a+b}{2}y \quad (4)$$

$$A_{hex} = \frac{3\sqrt{3}}{2}l_h^2 \quad (5)$$

where, in Eq. (4), a and b denote the top and bottom edges of the trapezoid, and y symbolizes the height (Figure 1(b)). Also, from Figure 1(b), it is noticed that b will be the sum of h and $4l_h$, while a equals $b - 2x$. Both x and y are obtained as:

$$x = (l + 2l_h) \sin \frac{\theta}{2} \quad (6)$$

$$y = (l + 2l_h) \sin \theta \quad (7)$$

Using Eqns. (6) and (7), the expressions for a and b simplify to:

$$a = (h + 4l_h) - 2(l + 2l_h) \sin \theta \quad (8)$$

$$b = h + 4l_h \quad (9)$$

From Eqns. (8) and (9), the total area of the unit cell (A_t) is thus obtained as:

$$A_t = (2h + 6l_h - l)(\sin \theta (l + 2l_h)) + 6\sqrt{3}l_h^2 \quad (10)$$

Next, the area fraction occupied by the hexagon elements, A_h , takes the form.

$$A_h = \frac{9\sqrt{3}l_h^2}{(2h+6l_h-l)(\sin 60(l+2l_h))+6\sqrt{3}l_h^2} \quad (11)$$

With the help of Eqns. (1), (2) and (11), the relative density of the HHRH can be varied to assess the effect of scaling the reinforcing elements on the overall performance of the auxetic structure.

Meanwhile, to assess the crashworthiness of the HHRH models, the following metrics are employed: (a) the peak stress (σ_p); (ii) the magnitude of energy absorption (E_d); (iii) the average stress between the peak stress and the densification stress (σ_{pl}); and (iv) the Poisson's ratio (ν). Each of these parameters is defined as follows [36, 52, 61, 62]:

$$E_d = \int_0^{\varepsilon_d} \sigma(\varepsilon) d\varepsilon \quad (12)$$

$$\sigma_{pl} = \frac{\int_{\varepsilon_p}^{\varepsilon_d} \sigma(\varepsilon) d\varepsilon}{\varepsilon_d - \varepsilon_p} \quad (13)$$

$$\nu = -\frac{\varepsilon_x}{\varepsilon_y} = -\frac{\bar{\Delta}L/L}{\varepsilon_y}, \text{ where } \bar{\Delta}L = (A_x + B_x + C_x + D_x)/4 \quad (14)$$

In Eq. (14), ε represents the crushing normal strain and $\sigma(\varepsilon)$ is the crushing normal stress experienced by the structure, which is obtained by multiplying the reaction force between the impactor and the structure to the initial cross-section area of the structure [56]. Besides, ε_p is the peak strain corresponding to the peak stress, while ε_d is the densification strain. The densification strain is defined as the point after which the crushing stress rises sharply

[57]. Concerning Eqn. (14), ε_x is the lateral strain along the x -axis and ε_y signifies the longitudinal strain along the y -axis (vertical direction). Moreover, $\bar{\Delta}L$ is calculated by averaging the lateral displacements of 4 symmetric nodes on both sides of the model as shown in Figure 3, while L is the initial lateral length of the structure.

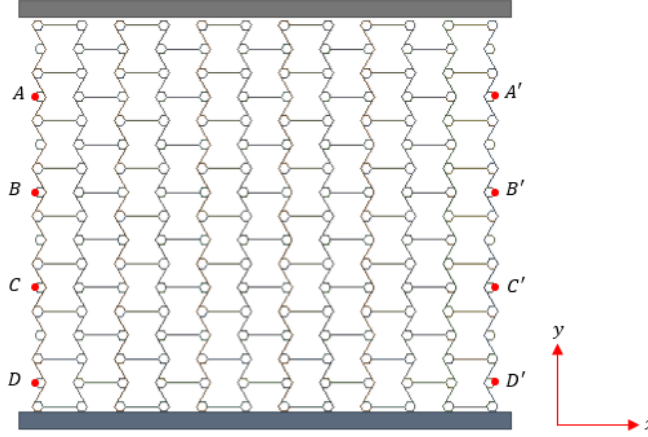


Figure 3: Calculating the average lateral displacement

2.3 Finite element simulation of the impact response

Numerical analysis of the mechanical performance of the novel auxetic structures to in-plane crushing is carried out using the nonlinear explicit finite element solver ANSYS/AUTODYN. In this model, the structure is sandwiched between two plates as shown in Figure 4. The bottom plate is fixed while the top rigid plate crushes the honeycomb structure at an impacting velocity, V , along the negative y -axis direction. The crushing speed is varied between 6-100 m/s in this study to capture the crushing responses associated with low, intermediate, and high velocities. An out-of-plane thickness of 8 mm is assigned throughout. Similar to [63], all investigated structures have 6 unit cells in the horizontal direction and 8 cells in the vertical direction to achieve reasonable global bulk properties.

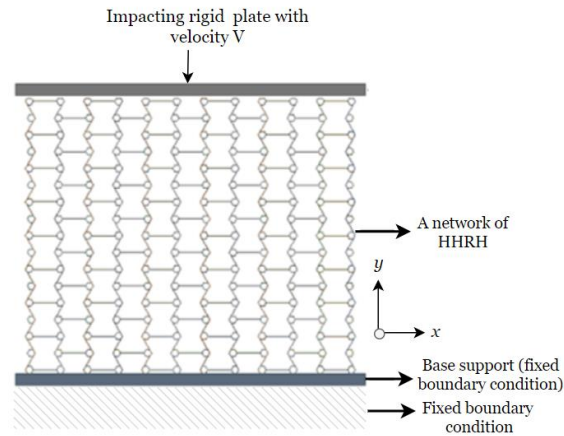


Figure 4: Schematics of the auxetic structure between the impactor and the fixed end

Aluminium alloy is selected as the solid material of the HHRH structure. With this, the following material properties are used: Young's modulus, $E = 71 \text{ GPa}$; Poisson's ratio, $\nu = 0.33$; yield strength, $\sigma_y = 280 \text{ MPa}$; and density $\rho = 2770 \text{ kg/m}^3$. Furthermore, an idealized elastic-perfectly plastic material behaviour is adopted in this model. The out-of-plane degrees of freedom are constrained for all nodes to prevent deformations along the z-direction. Moreover, to avoid the interpenetration of cell walls during dynamic crushing, a shell thickness factor of 1 is used along with automatic single surface contacts. A bonded contact is assigned between the structure and the bottom plate, while a frictional contact is employed between the impactor and the structure [52, 62]. To have a time-step size that achieved a balance between accuracy and convergence, a modal analysis was performed to determine the natural frequency of the structure. Eventually, the inverse of 20 times the 10th natural frequency (f_n^{10}) is used for the time-step [64]. Figure 5 demonstrates the f_n^{10} and the 10th mode shapes of each model.

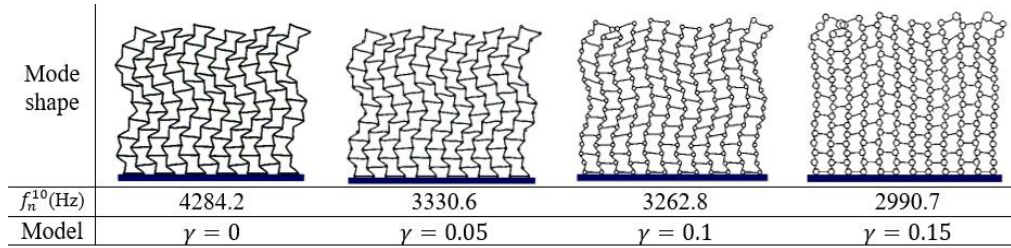


Figure 5: The estimated 10th natural frequencies for the models investigated.

2.4 Machine learning model for intelligent detection of impact events

2.4.1 Random forests modelling

Based on the output data accumulated from the FE numerical experiments on impact analysis, we undertook the implementation of a machine learning (ML) model. This bridges the gap between the forward problem of determining the impact response of the auxetics and the inverse problem of real-time reconstruction of the dynamic response for monitoring or detection purposes. Devised by Breiman [65], RF belongs to the family of ensemble supervised ML schemes whose base learner is a decision tree. Recognizing its capability and flexibility, several studies have employed RF for classification and regression tasks with high-dimensional feature spaces [66-69]. Consequently, the current study employs the regression mode of RF to develop a predictive model of the dynamic impact stress. This model is anticipated to be used as a baseline to trigger an alarm in case of an impact event or to discriminate between different classes of impact events.

2.4.2 Major steps of RF modelling, software package and hyperparameters

For this study, the RF modelling was carried out using the *randomForest* package within the R programming environment [70, 71]. The construction of RF is outlined next. Given a matrix of a training dataset (S) of n observations and p predictor variables, the development of the RF scheme features the following steps [72-74].

1. *Bootstrap sampling*. This involves drawing random samples (which may range from $b = 1 \dots B$), of size s from the original training dataset (\mathcal{L}).
2. *Growing of random forest trees*. This relates to the construction of hundreds (and at times thousands) of tree-based predictive models (t_b) using the bootstrap samples. Primarily, this involves two major sub-steps.
 - a. Fit a tree on a bootstrap sample (\mathcal{L}_b), where the tree consists of branches, internal nodes, and terminal nodes.
 - b. At each node of the tree, randomly select m subset of the p independent predictors for splitting. Here, the m selected predictors are tested as candidates for splitting and the predictor that yields the best split is chosen. This sub-step decreases the correlation between the trees in the forest.
 - c. With the best split determined, a cut point c_s is identified. With this, the data is split by sending observations with $x_{ij} < c_s$ to the left child node and the $x_{ij} > c_s$ to the right child node.
 - d. For each tree, sub-steps (a) - (c) are repeated until a terminal node is reached.
3. *Ensemble averaging*. Here the average of the observed target value at the terminal nodes of the collection of RF trees is outputted as the final predicted value. In short:
 - a. Collate the outputs of the ensembled $\{t_b\}_1^B$, where B is the total number of bootstrap samples.
 - b. Predict numerical observation at a new point \mathbf{x} by using:

$$f_{rf}^B(\mathbf{x}) = \frac{1}{B} \sum_{b=1}^B t_b \quad (15)$$

On the practical side, the above steps lead to some key hyperparameters that can be leveraged for the optimal performance of RF models [72, 75]. This includes, among others: (i) *sample size* – the number of observations that are drawn for each tree in step 1 above; (ii) *ntree* – the total number of trees in the random forest architecture; (iii) *mtry* – the number of predictors selected for splitting as highlighted in step 2a; and (iv) *nodesize* – the size of data points in a cell below which the cell is not split further.

2.4.3 Dataset, data splitting and performance measures

Overall, the dataset used for the RF modelling consists of 3523 observations with a total of 6 predictors and 1 outcome variable as listed in Table 2. The 6th predictor named velocity class takes on three values (*low*, *medium*, and *high*) and it is derived from the value of the impacting velocity (that is *low* = 6 m/s, *medium* = 20 m/s, and *high* = 100 m/s).

A core aspect of ML workflow is to split an original dataset into training and testing datasets. As part of this workflow, we experimented with the implication of using 60:40, 65:35, and 70:30 ratios of the training data to test data. Consequently, the performance of three RF models of the crushing response (named *CR-RF1*, *CR-RF2* and *CR-RF3*) is examined and contrasted. For these RF models, three of the hyperparameters (*ntree*, *mtry*, and *nodesize*) were tuned to maximize the generalization of the results [75]. Meanwhile, the estimated optimal hyperparameters, which are obtained via the grid search technique, were used to build the three RF models.

Table 2: Predictor and outcome variables

Variables	Definitions	Description
Predictors	h : The length of the horizontal edge of the unit cell (depicted in Figure 1a) (mm)	Continuous
	l : The length of the slanted edge of the unit cell (depicted in Figure 1a) (mm)	Continuous
	γ : The hierarchical scaling parameter	Continuous
	V : A vector of impact velocity (m/s)	Continuous
	ε : Dynamic nominal strains of past impact events	Continuous
	Velocity class	Categorical
Outcome	σ : Dynamic impact stress (MPa)	Continuous

At the heart of every ML modelling task is the central question of performance. For this reason, the predictive accuracy of the model was established by using the test dataset via the following metrics: coefficient of determination (R^2); the root mean squared error (RMSE); and the mean absolute error (MAE). These are defined as follows [76-78]:

$$R^2 = 1 - \frac{RSS}{TSS} \quad (16)$$

where RSS and TSS denote the residual sum of squares and the total sum of squares, respectively. They are defined as:

$$RSS = \sum_{i=1}^n (y_i - f_i)^2 \quad (17)$$

$$TSS = \sum_{i=1}^n (y_i - \bar{y})^2 \quad (18)$$

$$RMSE = \sqrt{\frac{1}{n} \sum_{i=1}^n (y_i - f_i)^2} \quad (19)$$

$$MAE = \frac{1}{n} \sum_{i=1}^n |y_i - f_i| \quad (20)$$

where \bar{y} symbolizes the average value of the actual data, and n is the number of experimental data. Besides, y_i and f_i are the i^{th} actual and predicted values of the outcome variable, respectively.

3. Result and discussion

3.1 Validation and convergence studies

As a starting point, several validation studies were conducted to substantiate the accuracy of the simulation setup. Here, two layers of validation are presented.

First, we validate the negative Poisson's ratio effect of a basic re-entrant unit cell that is statically loaded and compared the results with the work of Zied, et al. [48]. Figure 6(a) describes the major geometric features of the re-entrant unit cell. A representative model of the loaded unit cell is shown in Figure 6(b). As with the simulations in later sections, the simulation of the unit cell is accomplished with ANSYS using a collection of shell elements (SHELL181) to be consistent with Zied, et al. [48]. All later computations are based on the following properties: $E = 210 \text{ GPa}$, $\nu = 0.3$, thickness of l ($t_l = 3 \text{ mm}$), thickness of h ($t_h = 3 \text{ mm}$), $\theta = -23^\circ$, width of the unit cell, $w = 8 \text{ mm}$. For the static simulation, the unit cell is subjected to a tensile remote force at the top end along the y -axis, while the base is fixed. Consequently, the Poisson's ratio is computed as the ratio of the lateral extensional strain (ε_x) against the longitudinal extensional strain (ε_y). Both strains are found using the directional displacements of reference points on the unit cell, which is consistent with the approach used for the computational results in the other sections that follow. As an example, the transverse strain is calculated as shown in Figure 6(b), while the longitudinal extensional strain is found using the ratio of the average longitudinal displacements of vertical reference points on the unit cell against the initial height H .

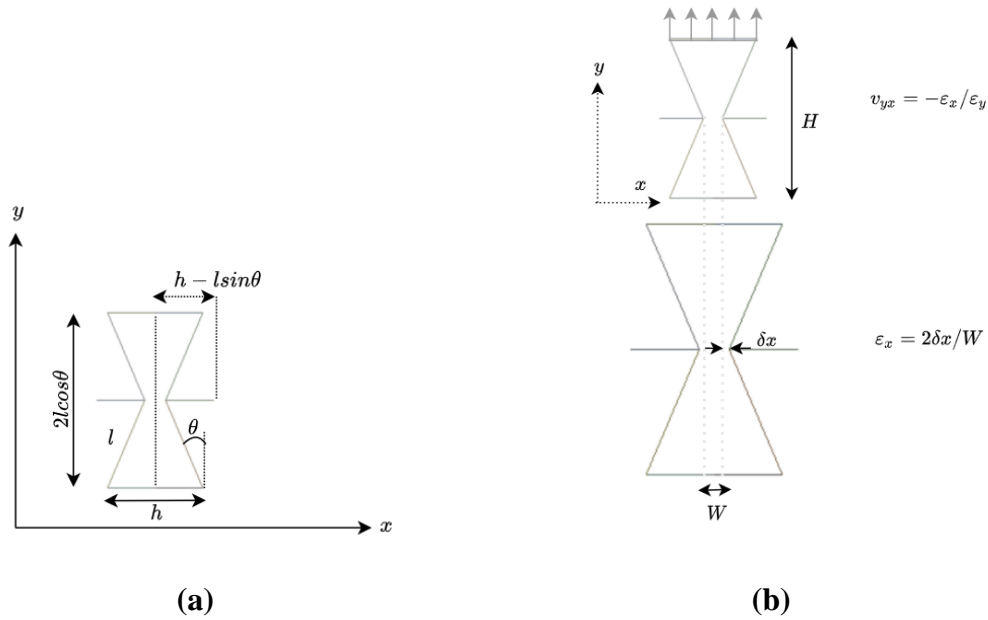


Figure 6: (a) Basic geometric dimensions of the re-entrant unit cell; (b) evaluation of the strains for Poisson's ratio calculation.

It's important to highlight that to avoid the Saint-Venant effect [57], the final simulated structure is modified as shown in Figure 7(a) so that the unit cell is positioned at the centre. Furthermore, to restrict the deformation to in-plane tension/compression behaviour, the rotational degrees of freedom along with the out-of-plane translational degree of freedom of all nodes of the shell elements are constrained. Table 3 compares the results from the current study with those reported in [48]. An example of the deformed finite element model is shown in Figure 7(b).

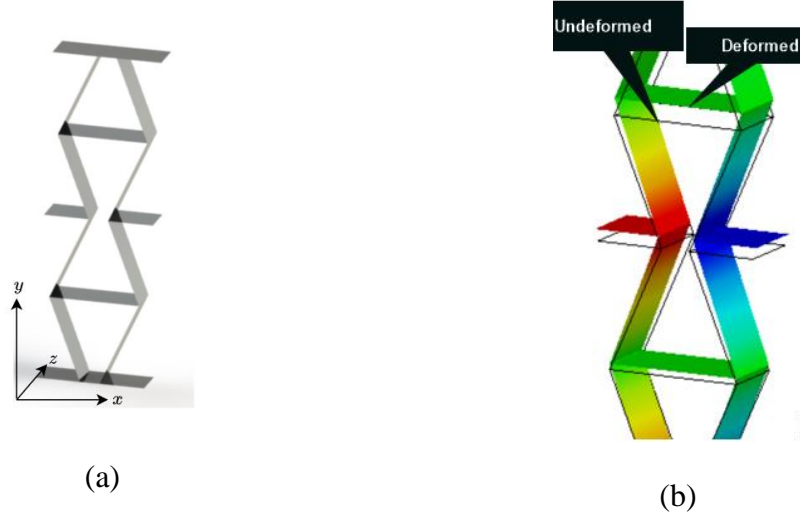


Figure 7: (a) Model of the undeformed unit cell; (b) illustration of the deformed pattern of the re-entrant unit cell after loading.

Table 3: Negative Poisson's ratio

<i>Rib length</i>	<i>Major Poisson's ratio (v_{yx})</i>		
	Present	Numerical [48]	Experiment [48]
15	-2.68	-2.79	-2.99
25	-2.95	-2.93	-3.10
30	-3.03	-2.99	-3.20
40	-3.47	-3.42	-3.42
60	-3.69	-3.62	-3.65

Overall, it is observed from the table that a good agreement is found between the current study with the experimental and numerical results reported in [48]. The table further shows that, by keeping the rib angle (θ) constant, the Poisson's ratio decreases (becomes more negative) as the rib length increases. Technically, this can be attributed to reduced stiffness of the structure with increased rib length and indicates that the Poisson's ratio can be tuned by adjustment of the geometric parameters. Furthermore, the largest percentage difference between the current study and the numerical computations is roughly 4%. This small deviation can be explained by the fact the current study employed the ANSYS's shell element SHELL181, which differs in stiffness from the ANSYS's legacy SHELL99 element type employed in [48]. As for the comparison with the experimental data, a slightly higher percentage difference of 11% is obtained. This deviation can be attributed to the difference between the experimental setup and the simplified boundary conditions employed for the simulation.

Proceeding to the next validation, we consider a network of re-entrant unit cells subjected to impact. For this, a comparison with the work of Hou, et al. [79] is undertaken. The model (8 cells by 11 cells), which is a basic re-entrant structure with no hierarchical feature, is crushed vertically at a velocity of 100 m/s. Representative plots of the crushing response at different crushing strains, ε , and the stress-strain graph are shown in Figure 8 and Figure 9, respectively. The layer-by-layer deformation modes at the proximal end and the general pattern of deformation shown in Figure 8 are consistent with those reported in [79]. Moreover, the first peak stress and the plateau stress, with corresponding values of 92.4 MPa and 3.62 MPa differed by less than 2% from those reported by Hou, et al. [79].

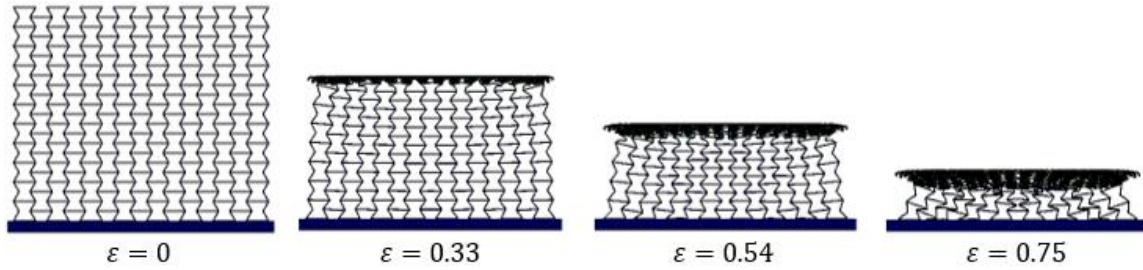


Figure 8: Crushing response of the validation model at different crushing strains

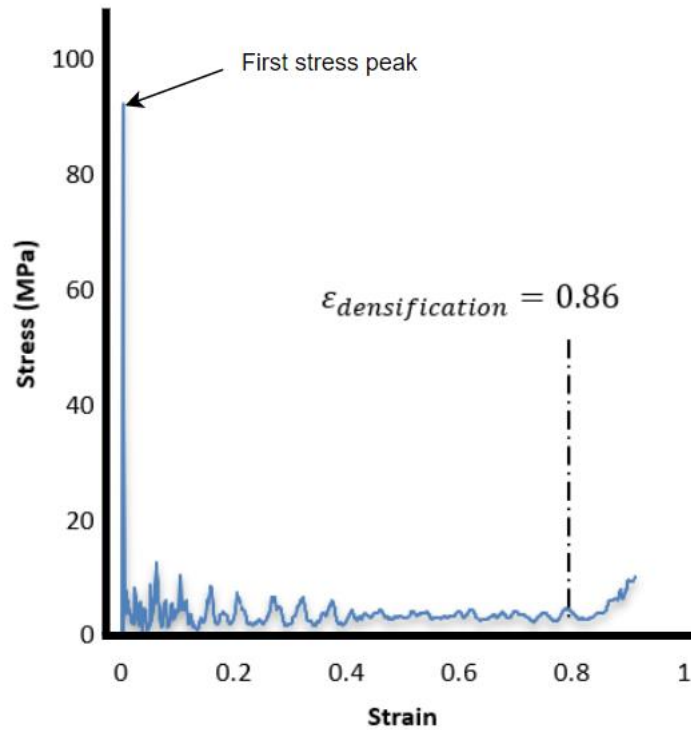


Figure 9: Stress-strain curve of the validation model

For subsequent analyses involving the hierarchical re-entrant structure, a mesh convergence analysis is performed to choose a suitable mesh size. Figure 10 shows the convergence results, indicating that a mesh size of 0.3 mm is appropriate to balance the computational cost and accuracy of the dynamic stress. This mesh size is found to be consistent with other studies, for instance [80].

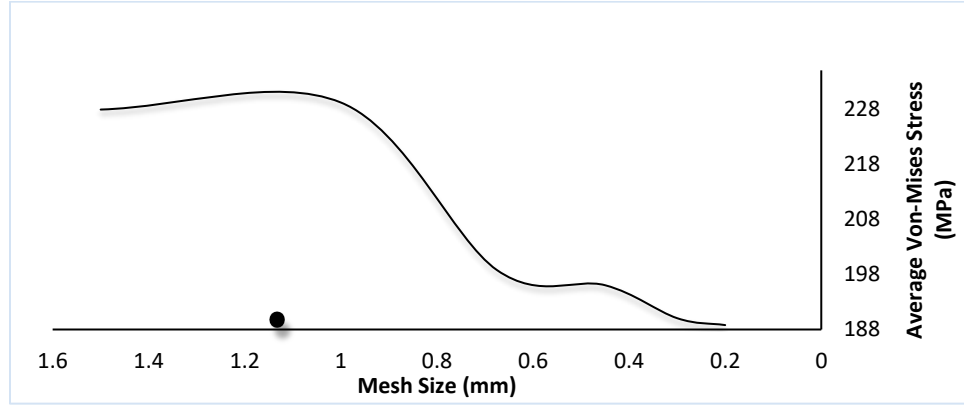


Figure 10: Mesh independent analysis for the hierarchical re-entrant

3.2 Crushing response of hierarchical re-entrant auxetics

3.2.1 Deformation modes with different scaling factors at a low, medium and high impacting velocity

Crushing velocity influences the global deformation modes of cellular materials as reported in previous studies [62, 81]. In the case of hierarchical structure, a different magnitude of the scaling factor (defined in section 2.1) also leads to different crushing strengths. In what follows, the effect of crushing speed on three of the models with varying scaling factors is reported. All models are crushed along the negative y -direction and the global deformation is observed. Besides, ε represents the global strain of the models under the impacting velocity.

Figure 11 and Figure 12 respectively depict representative deformation modes and the stress-strain curves involving the nominal axial stress vs nominal axial strain of three HHRH models under the 6 m/s impacting velocity. Specifically, Figure 11(a) shows the deformations at four selected strain points for $\gamma = 0.15$ (the HHRH with the biggest hierarchical elements). This model experiences the greatest distortion. Besides, at a low strain value, a V-shaped band starts to develop, which soon disappeared as crushing strain increases because of the larger-sized hierarchical elements. As a result of the larger hexagons when $\gamma = 0.15$, the ribs of the ensuing structure are not long enough to generate the kind of alignment observed when $\gamma = 0.1$ and 0.05 . Instead, the hexagons become stacked on top of each other. Further crushing causes the stacked hexagons to buckle and eventually densify. This then generates a response that appears to be a composite of the hexagonal unit cell and that of the re-entrant unit cell. The corresponding impact stress-strain curve is portrayed in Figure 12(a). The plot reveals the apparent two-stage local deformation modes with the transition strain located at $\varepsilon = 0.3$. Stage 1 is dominated by

bending and rotational winding of the diagonal ribs, while stage 2 mostly experiences buckling of the stacked hexagon elements.

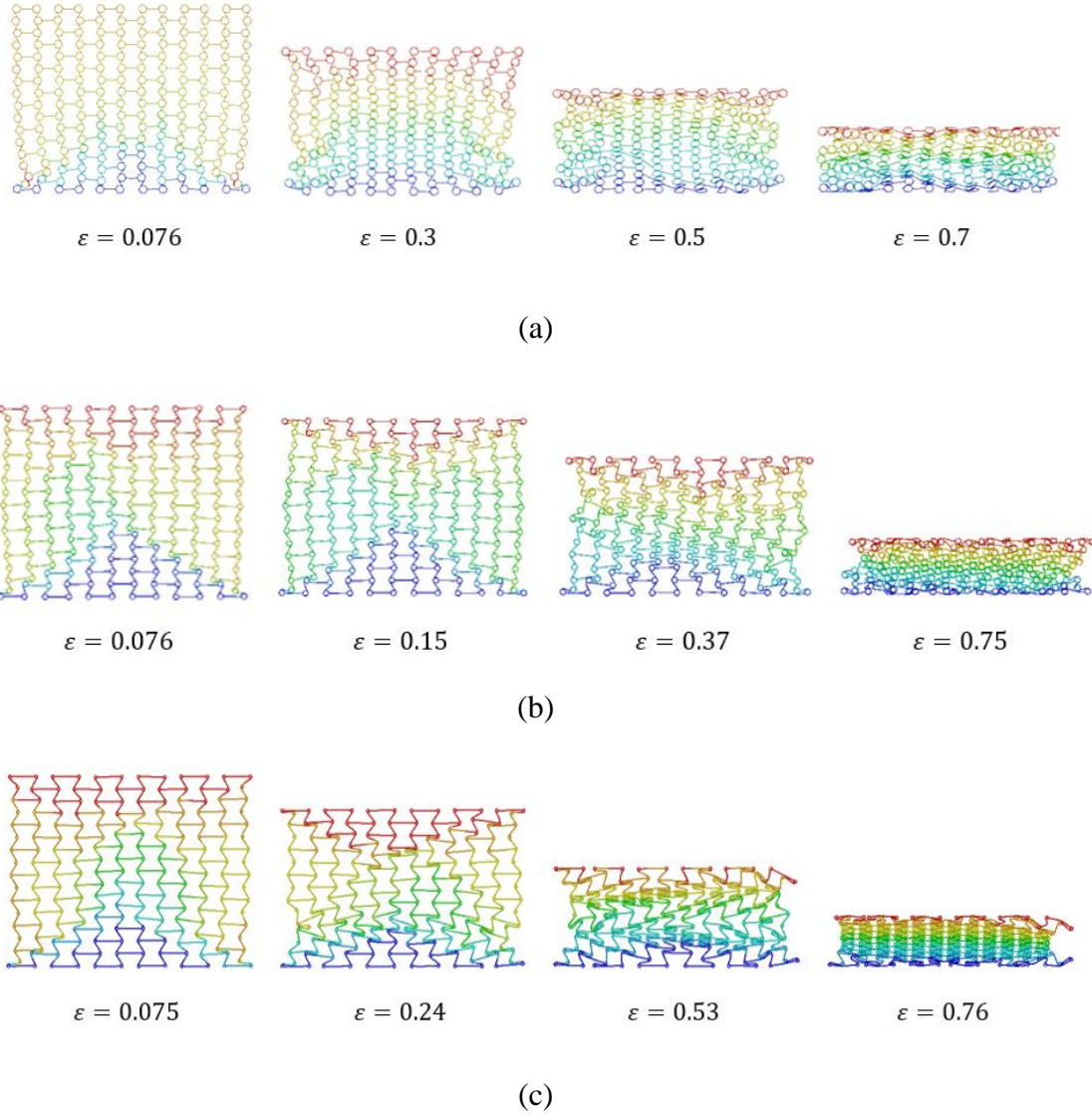


Figure 11: Crushing response of the different models at a crushing velocity of 6 m/s: (a) $\gamma = 0.15$; (b) $\gamma = 0.1$; (c) $\gamma = 0.05$.

Figure 11 (b) is the deformation mode for $\gamma = 0.1$. Here the appearance of the V-shaped deformation band at the distal end is noticeable. As the strain increases, a second V-shaped deformation band also appears at the proximal end of the impactor, oriented in the opposite direction of the distal end. Further increase in the crushing displacement leads to the densification of the structure. In Figure 11(c), when $\gamma = 0.05$, a crushing response similar to when $\gamma = 0.1$ is also observed. Essentially, the small size of the hexagonal elements in these two cases generates a higher rotational stiffness. This is similar to the observation reported by [49], although for a different auxetic design. Meanwhile, as the crushing

progresses, some of the struts of the main re-entrant sub-cell start to bend around the corner hexagonal elements, creating a rotational deformation pattern that bears semblance to that of chiral type auxetic structures.

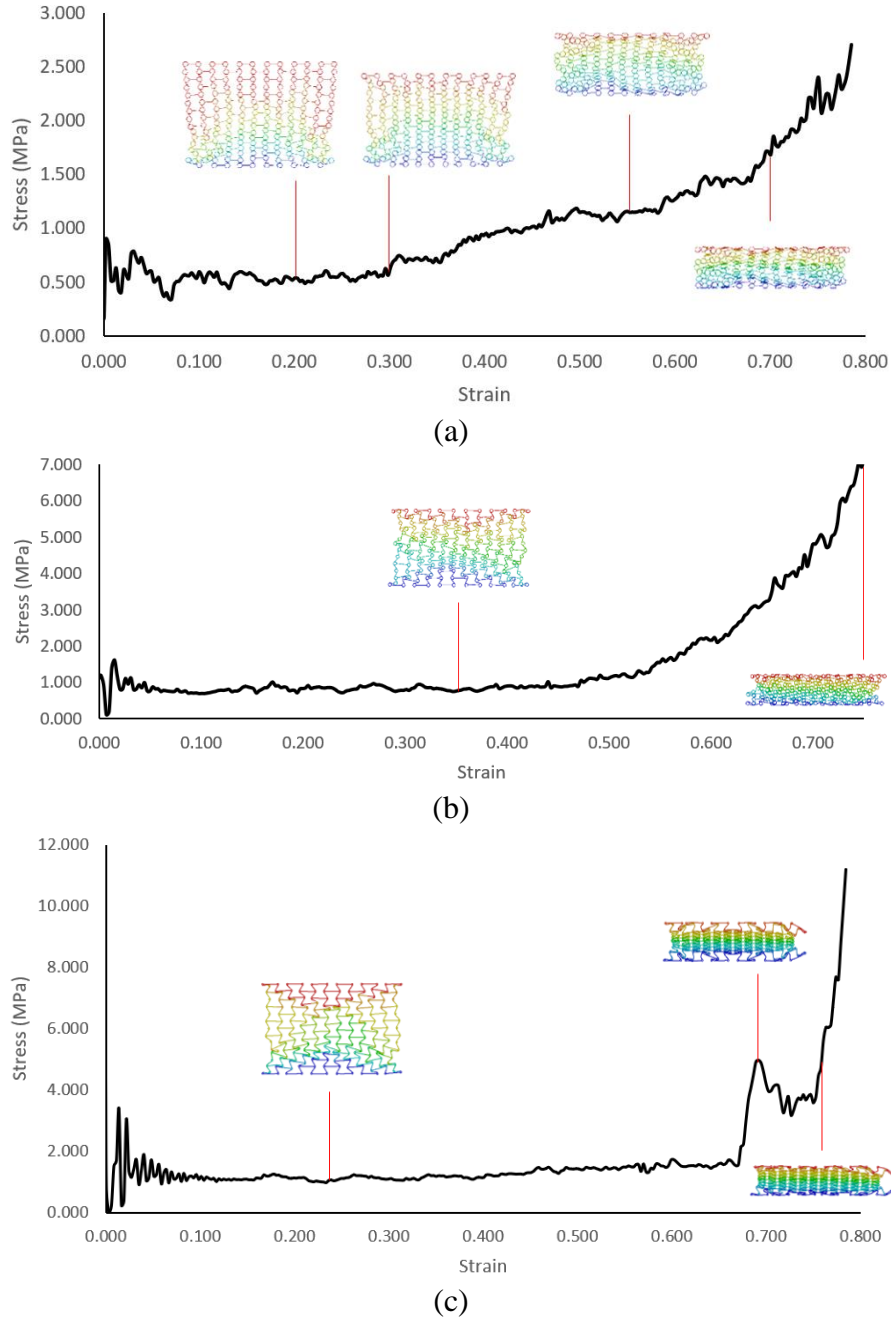


Figure 12: Crushing response of the HHRH: (a) $\gamma = 0.15$; (b) $\gamma = 0.1$ and (c) $\gamma = 0.05$ structure at different stages in the stress-strain curve at a crushing velocity of 6 m/s.

The corresponding stress-strain curve (nominal axial stress vs nominal axial strain) for Figures 11(b) and (c) are shown in Figures 12(b) and (c), respectively. As depicted in these figures, these models have a single notable plateau region. Further, as the curves show, at

the final stage of the crushing process, the structures are densified leading to a sharp rise in the crushing stress. Besides, from the three stress-strain curves, it is observed that the first peak stress upon impact is highest for $\gamma = 0.05$ and lowest for $\gamma = 0.15$. Also, for $\gamma = 0.05$ a sudden rise and drop of stress can be observed at a strain value $\varepsilon = 0.69$ partly due to alignment of some diagonal ribs at the final row. The buckling of these aligned cell edges causes a temporary rise in crushing stress after which the structure densifies causing the stress to rise sharply again.

Under the impacting velocity of 20 m/s, Figures 13 and 14 represent the deformation modes and the stress-strain response curves at increasing strain levels.

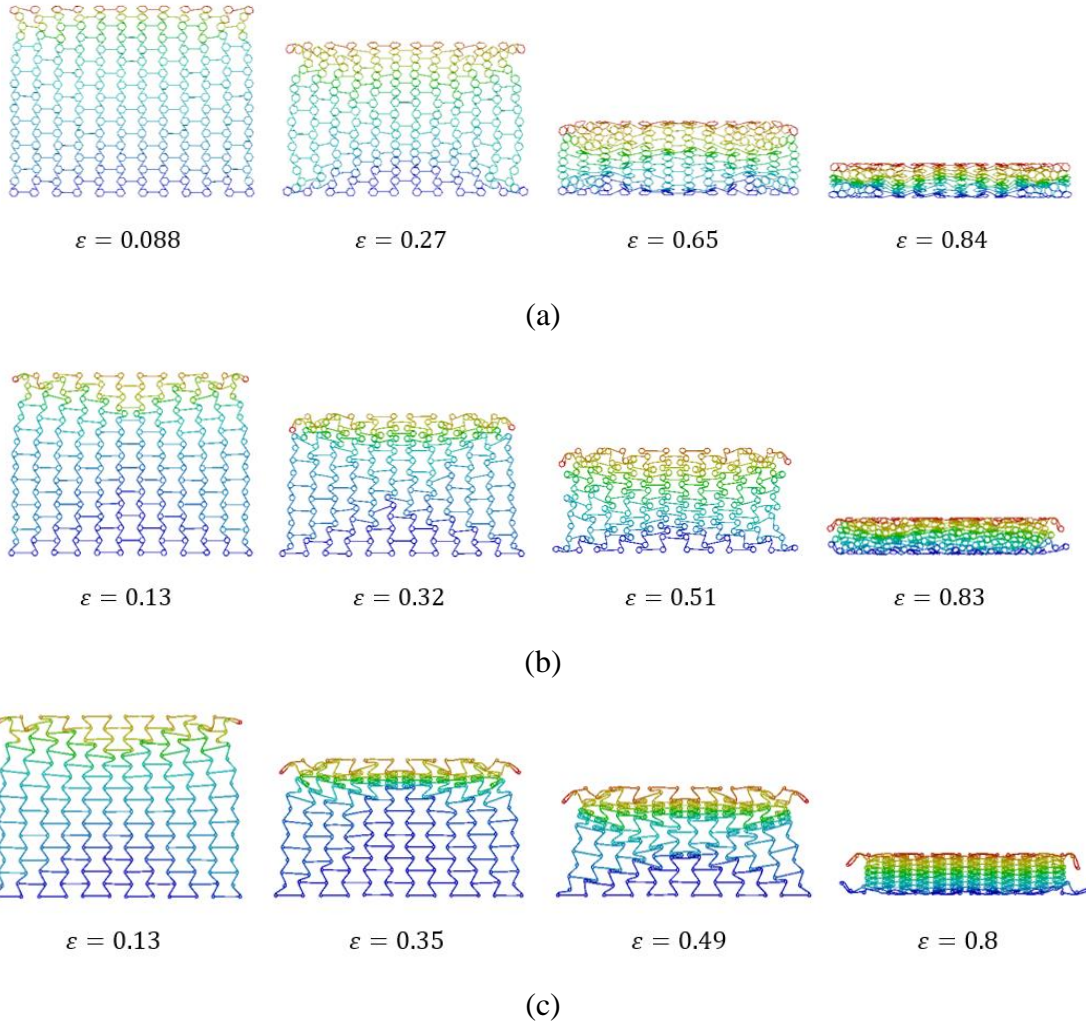


Figure 13: Crushing response of the different models at a crushing velocity of 20 m/s: (a) $\gamma = 0.15$; (b) $\gamma = 0.1$; (c) $\gamma = 0.05$.

From Figure 13, it is noticed that all three models experienced localized deformations at the medium strain level. However, the unit cells of the model with $\gamma = 0.15$ (Figure 13a) experienced more sliding deformations compared to the others (Figure 13b and c). Moreover, for $\gamma = 0.05$, as crushing strain increases, first there is a clustering of the unit

cell towards the centre ($\varepsilon = 0.49$) due to auxetic effect and then finally the alignment of the unit cells. This alignment of the unit cell produced prolonged plateau stress after the densification stage takes place as reflected in Figure 14. Further, from Figure 14, it is seen that of the three models, the peak resistance stress is highest for the case when $\gamma = 0.05$, follow by $\gamma = 0.1$, and then $\gamma = 0.15$.

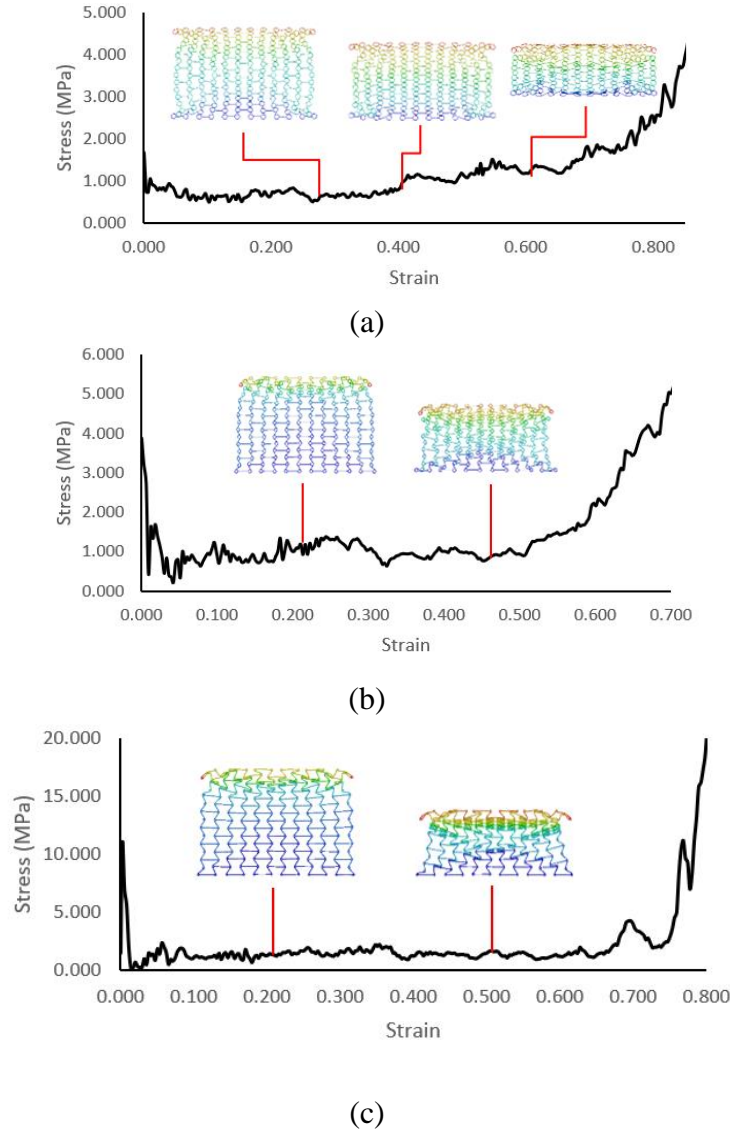


Figure 14: Stress-strain curves of three HHRH at a crushing velocity of 20 m/s: (a) $\gamma = 0.15$ (b) $\gamma = 0.1$ and (c) $\gamma = 0.05$.

For the higher crushing speed of 100 m/s, Figures 15 and 16 signify the deformation modes and the response curves, respectively. Here, as shown in Figure 15, the inertia effects dominate and there is a gradual layer-by-layer deformation that aggregates at the proximal end and then propagates as the crushing progress until the HHRH structures densify. Also, due to the layer-by-layer deformation mode, the stress-strain curves in Figure 16 indicate

that all three structures experience very high oscillations around a single plateau stress, consistent with [79]. As with the low and medium-impacting velocity, the model with $\gamma = 0.05$ experience a high resistant stress that is almost twice that of the other two models.

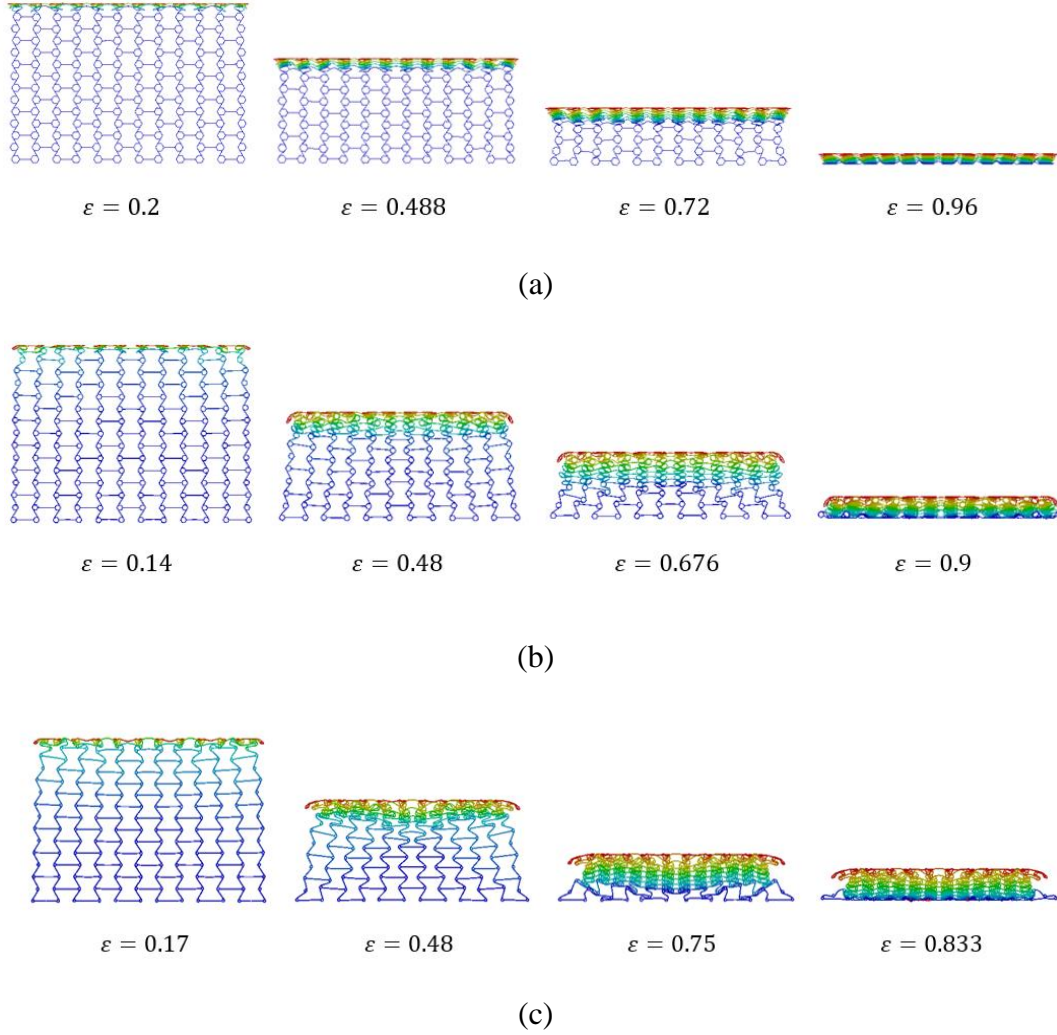
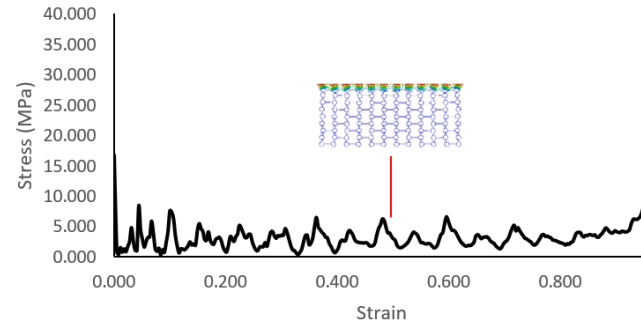
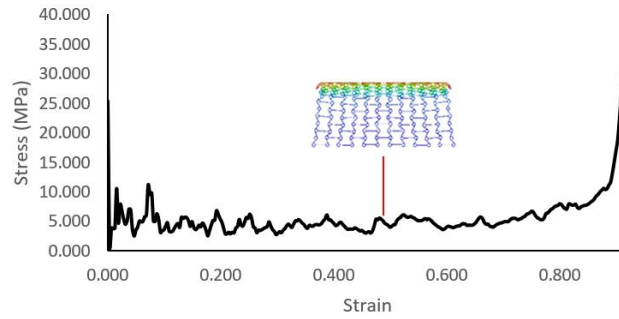


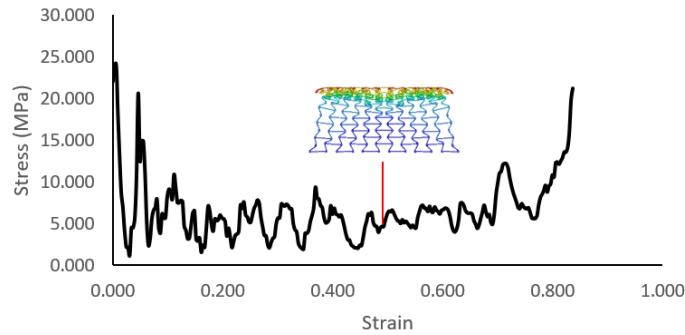
Figure 15: Crushing response of the different models at a crushing velocity of 100 m/s: (a) $\gamma = 0.15$; (b) $\gamma = 0.1$; and (c) $\gamma = 0.05$.



(a)



(b)



(c)

Figure 16: Crushing response of the HHRH structures at different stages in the stress-strain curve at a crushing velocity of 100 m/s: (a) $\gamma = 0.15$; (b) $\gamma = 0.1$ and (c) $\gamma = 0.05$

3.2.2 Evaluations of crashworthiness

Several indicators are used for assessing the crashworthiness of structures. Peak stress, σ_p , is one of these indicators [82]. Others include plateau stress and densification strain as summarized in Table 4. From this table, it is observed that the HHRH structure reduces σ_p compared to the traditional re-entrant hexagonal structure ($\gamma = 0$). Overall, the results in

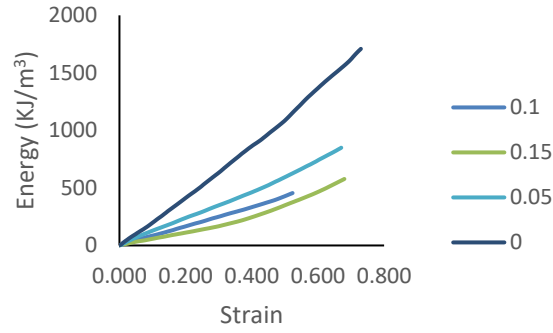
the table show that increasing γ reduces the σ_p experienced by the HHRH structure, which is related to the ability of hexagon structures in reducing σ_p [46].

Table 4: Crashworthiness parameters

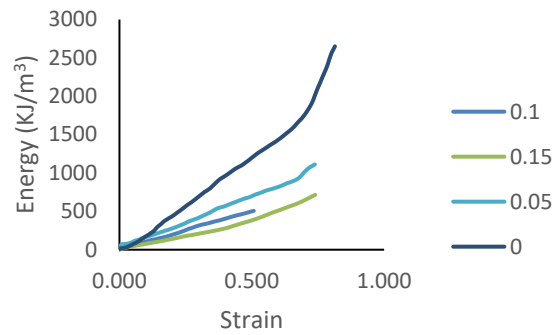
Velocity, V (m/s)	The hierarchical scaling factor (γ)	Peak Stress, σ_p (MPa)	Plateau Stress, σ_{pl} (MPa)	Densification Strain, ε_d
6	0	3.936	2.325	0.730
	0.05	4.362	1.258	0.670
	0.10	1.614	0.833	0.470
	0.15	0.901	$1^{st} = 0.549$	0.680
			$2^{nd} = 1.077$	
20	$\gamma = 0$	11.704	3.240	0.814
	$\gamma = 0.05$	10.898	1.465	0.738
	$\gamma = 0.1$	3.878	0.984	0.508
	$\gamma = 0.15$	1.670	$1^{st} = 0.684$	0.740
			$2^{nd} = 1.284$	
100	$\gamma = 0$	54.582	8.569	0.763
	$\gamma = 0.05$	24.156	5.981	0.765
	$\gamma = 0.1$	25.396	4.906	0.833
	$\gamma = 0.15$	16.834	3.015	0.918

Meanwhile, from Table 4, the peak stress is also noticed to intensify as the crushing velocity increases. For instance, at $V = 6 \text{ m/s}$, σ_p values of 3.936, 4.362, 1.614 and 0.901 MPa were recorded when $\gamma = 0, 0.05, 0.1$ and 0.15 , respectively. The lowest value of 0.901 MPa, recorded when $\gamma = 0.15$, reduced σ_p by 79.34% and 77.11% when compared to models with $\gamma = 0$ and $\gamma = 0.05$ respectively. A similar trend is observed under the medium and high impacting velocities. For instance, the lowest peak stress values of 1.670 MPa and 16.834 MPa were observed for the model with $\gamma = 0.15$ under the impacting velocities of 20 m/s and 100 m/s. Both values are lower by around 85.7 % and 69.2 % than that of the traditional re-entrant structure.

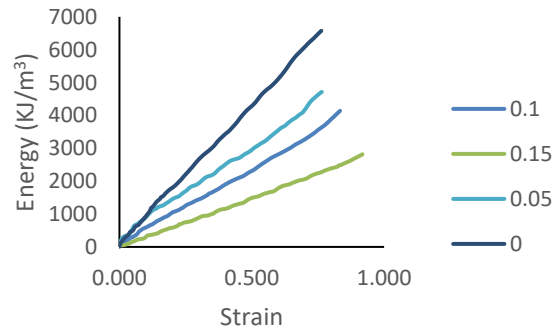
Another measure of crashworthiness is the energy absorbed per unit volume, E_d . This is represented by the area under the stress-strain curve before densification. Figure 17 illustrates the variation of this for the models at low, medium and high velocities, along with that of a re-entrant hexagonal model for comparison. As can be seen in this figure, independent of crushing velocity, E_d increases with increased crushing strain as more cell walls deform, which is in line with [36].



(a)



(b)



(c)

Figure 17: Accumulated energy absorption per unit volume for the different models at various crushing velocities: (a) 6 m/s; (b) 20 m/s and (c) 100 m/s.

During the low-velocity crushing, bending of the cell walls, initially about corner hinges and then winding around hexagon elements, is attributed to what creates most of the plastic deformation mechanisms utilized for energy absorption when $\gamma = 0.05$ and 0.1 . However, when $\gamma = 0.15$, one more energy absorbance mechanism is present, and that is the buckling of the stacked hexagon structure creating more plastic deformations. Consequently, the stacked hexagons will have an increased effective wall thickness at the top and bottom cell

walls due to the folding of slanted ribs in between the hexagon elements, yielding an increased second σ_{pl} , which is about 96.2% higher than the first σ_{pl} as indicated in Table 4. Further, when $\gamma = 0.15$, the total absorbed energy (577.8 kJ/m^3) is higher than when $\gamma = 0.1$ by about 46.35%. It should also be noted that the hexagon elements did not collapse at low and medium velocities when $\gamma = 0.05$ and 0.1 , as observed in Figure 12 and Figure 15, due to the increased effective wall thickness and given their small size, requiring very high crushing forces to further crush the structure. This causes early densification, reducing the area under the stress-strain curve. As γ reduces, the cell wall thickness increases to balance $\Delta\rho$ and as a result, cell walls will require more force to bend and deform. This is reflected by the increased σ_{pl} for $\gamma = 0.05$ and 0 by 16.8% and 115.9% respectively when compared to the 2nd σ_{pl} of $\gamma = 0.15$. This increased σ_{pl} will increase the area under the stress-strain curve causing an increase in E_d .

At $V = 20 \text{ m/s}$, a similar trend is observed where the highest $E_d = 2651 \text{ kJ/m}^3$ is dissipated when $\gamma = 0$, followed by $E_d = 1111 \text{ kJ/m}^3$ absorbed by the HHRH structure with $\gamma = 0.05$. At this velocity, the $\gamma = 0.15$ model is still able to outperform the $\gamma = 0.1$ model despite reduced wall thickness, with $E_d = 715 \text{ kJ/m}^3$, a 41% increase in energy absorption performance. The slight increase in E_d performance when $\gamma = 0.1$ compared to $\gamma = 0.15$ is assumed to be due to inertia effects starting to take effect with increased velocities, allowing more of the structure to collapse and incur plastic deformations to enable more energy absorbance. Further, when crushing velocity increases to 100 m/s , the global deformation mode is dominated by inertia effects causing a layer-by-layer collapse pattern.

All in all, the above indicates the existence of tradeoffs. Specifically, at the same $\Delta\rho$, the addition of the hexagonal elements mitigates the impact stress in HHRH. As a result, the HHRH structures perform better than the traditional re-entrant structure by reducing the initial σ_p . However, to benefit from the energy absorption capability of the parent auxetic structure, a careful balance is required between the size of the hierarchical hexagon elements and the parent auxetic unit so that the auxetic property of the parent unit cell is not lost.

3.2.3 Poisson's ratio

This section deals with the investigation of how the scale of the reinforcing hexagonal element influences the auxetic behaviour of the HHRH structure. For this, the Poisson's ratio, ν , at different axial crushing strains was computed at crushing velocities of 6 and 100 m/s . For brevity's sake, the following reported results focused on the variation of the major Poisson's ratio (that is ν_{yx}). Under the crushing velocity of 6 m/s , all models followed a similar trend where initially a sharp drop in Poisson's ratio is recorded due to initial shrinkage as revealed in Figure 18. It is noticed from the figure that the Poisson's ratio increases in absolute value as the strain increases, which aligns with other studies [28]. For this study, the minimum ν_{yx} values recorded were -0.62 , -1.15 , -1.85 and -2.29 when $\gamma = 0.15$, 0.10 , 0.05 and 0 respectively. When $\gamma = 0$, the structure experiences the minimum

drop in ν_{yx} , increasing with bigger reinforcing element as expected due to the hindering of the diagonal ribs folding process.

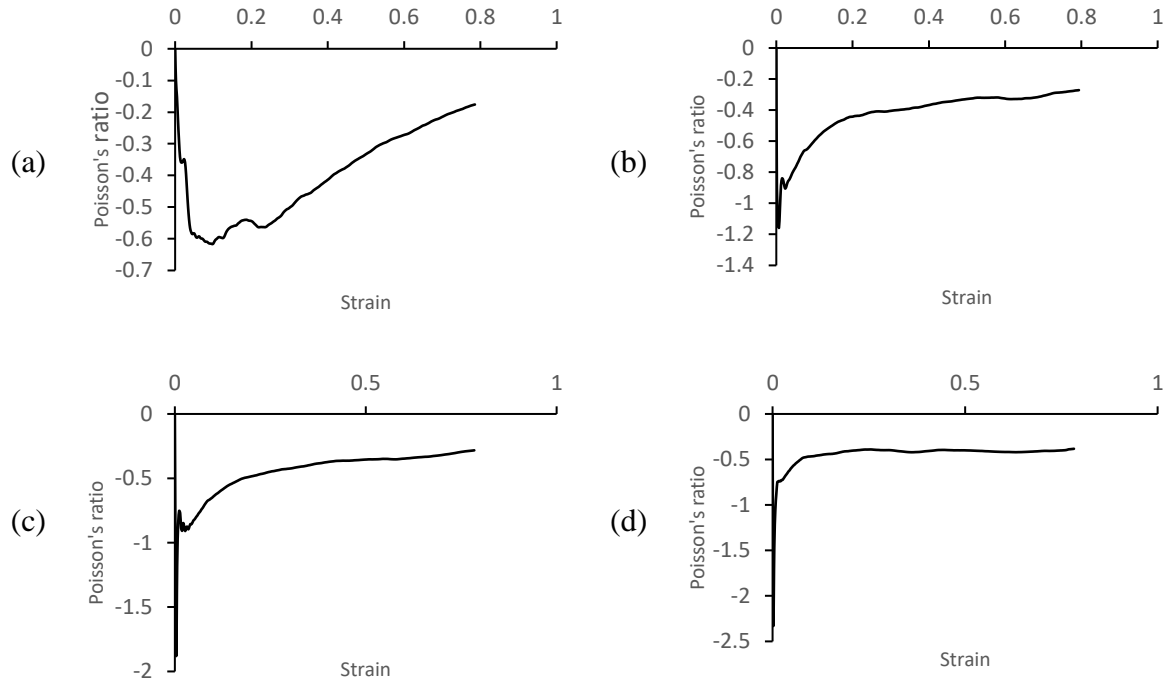
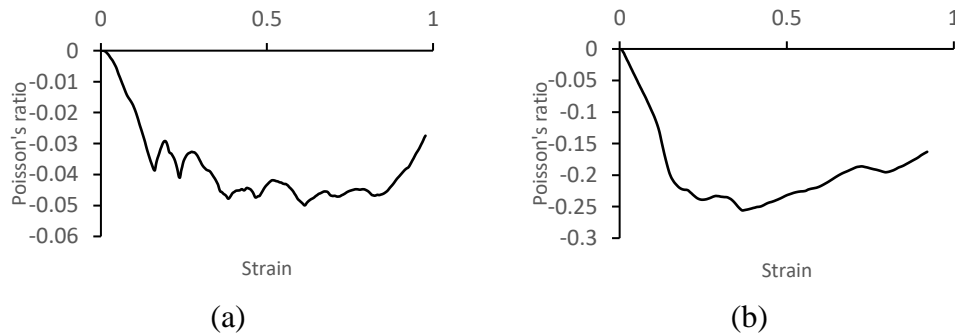


Figure 18: Poisson's ratio vs crushing strain at a crushing velocity of 6 m/s: (a) $\gamma = 0.15$, b); $\gamma = 0.1$ (c) $\gamma = 0.05$, (d) $\gamma = 0$.

It is observed that below a crushing strain of 0.05, the model with $\gamma = 0.15$ has the least NPR performance while that with $\gamma = 0.05$ demonstrates the best performance followed by 0.1 and 0 respectively. The effect of the high impacting velocity of 100 m/s is provided in Figure 19. It is noted that for this scenario, the initial sharp drop in Poisson's ratio is not apparent but rather, a more gradual decreasing-increasing ν_{yx} curve is obtained for all structures. The minimum ν_{yx} values recorded were -0.05, -0.26, -0.36 and -0.29 when $\gamma = 0.15, 0.10, 0.05$ and 0 respectively, suggesting an overall drop in auxetic performance at high crushing velocities consistent with the observation by Logakannan, et al. [83].



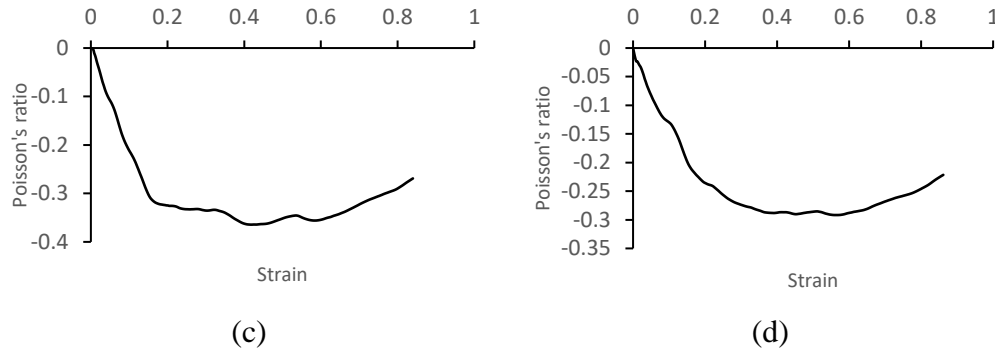


Figure 19: Poisson's ratio vs crushing strain at a crushing velocity of 100 m/s: (a) $\gamma = 0.15$; (b) $\gamma = 0.10$; (c) $\gamma = 0.05$; (d) $\gamma = 0$.

Another notable observation from the plots in Figure 19 is that during a crushing strain range of $0.2 \leq \varepsilon \leq 0.8$, the model with $\gamma = 0.15$ exhibited the least NPR effect with an average $\nu = -0.043$. This can be explained by the increased size of hexagon elements which will reduce the length of the slanted ribs and hence lower the NPR effect created by the folding of diagonal ribs. The best auxetic performance at 100 m/s is demonstrated by the $\gamma = 0.05$ model with an average $\nu = -0.339$, a 23.3% improvement when compared to the regular re-entrant structure. This improvement in auxetic performance can be attributed to the extra local deformation mode introduced by the addition of hexagon elements, where the winding of diagonal ribs around the hexagon elements tends to further increase the lateral shrinkage of the HHRH structure.

3.3 Random forests modelling results

3.3.1 Outcome of stratified sampling

As highlighted in section 2.4.3, three partition ratios are investigated leading to three random forests (RF) models of the crushing response, namely *CR-RF1*, *CR-RF2* and *CR-RF3*. For each of the partitions, we embraced the idea of stratified resampling via the *caret* package during the splitting phase of the data [84]. This is to ensure similar distribution between the training and test datasets. A representative plot of the stratified training and testing data is depicted in Figure 20 based on *CR-RF1*, which demonstrates a balanced distribution. But the plots also show that the feature space of the outcome variable is multi-modal, which can be quite challenging for non-robust ML schemes.

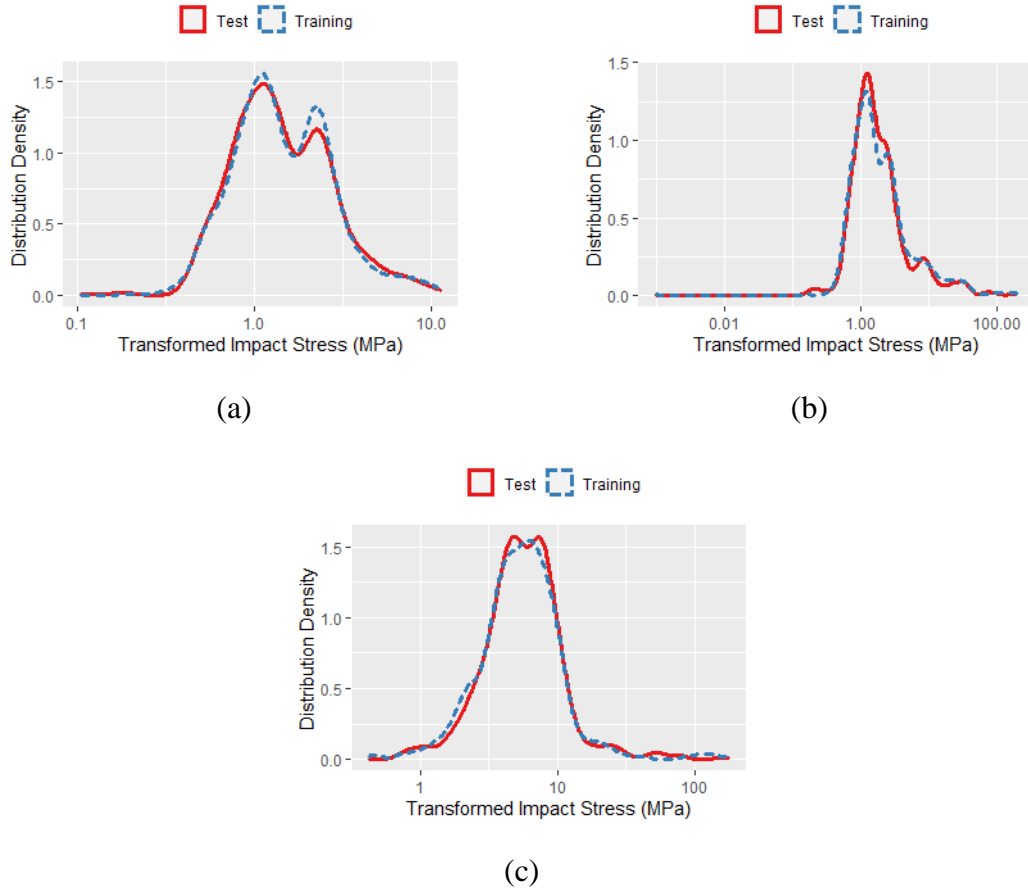


Figure 20: Effect of stratification to ensure analogous distribution of the test and training data: (a) 60:40 partition ratio; (b) 65:35 partition ratio; and (c) 70:30 partition ratio.

3.3.2 RF model optimization and performance metrics

With the stratified sampling completed, each training data set is deployed to fit an RF model, during which it encodes the interactions between the input variables and the various nonlinear features of the impact stress response curve. Meanwhile, for each RF model (*CR-RF1*, *CR-RF2* and *CR-RF3*), a grid search is performed to choose the best performing combination of hyper-parameters in terms of the number of trees, tree complexity and the subset of features to be considered at each node split (m_{try}). Table 5 highlights the best combinations of values determined for building a high-performing ensemble of RF trees for this study.

Table 5: Best performing choice of random forest parameters

RF parameters	Optimal choice
<i>Number of trees (ntree)</i>	250
<i>Number of random split points (nsplit)</i>	10
<i>No. of variables tried at each split (mtry)</i>	5
<i>Forest terminal node size</i>	1
<i>Resampling used to grow trees</i>	Sampling without replacement
<i>Resample size used to grow trees</i>	63.2% of the training observation

Using the parameter values indicated in Table 5, the out-of-bag (OOB) error rate is used to assess the performance of the model and to estimate variable importance, which is one of the unique upsides to working with RF [85]. Figure 21 depicts the variation of the error rate for each model. To provide more context about the OOB, in the building of the RF model, each tree is grown on a bootstrap sample as explained in section 2.4.2. For this reason, a few data points, known as OOB observations, are left out of the growing process of each tree. Consequently, these OOB data records are used internally to both estimate the generalization error of the random forest and to assess the significance of each predictor variable [86]. Premised on this, Figure 21 indicates the model with the 70:30 partition ratio (*CR-RF3*) achieves the lowest error rate among the three models, as seen in Figure 21(c). However, the plots in Figure 21 (a) – (c) also show that the error rates for all three models stabilize with roughly 250 trees. Figure 21 (d) illustrates the ranking of the predictor variables on the performance of *CR-RF3*. It is seen from this plot that the crushing strain is the most dominant factor in determining stress. Other geometric features defining the unit cell topology, l , h and l_h are all found to be of similar average importance. Interestingly, the variable importance plot suggests that the impacting velocity has a minimal influence on the predictive strength of the RF. However, given that the velocity implicitly contributes to the level of the strain, then this observation that the velocity has a minimal influence on the predictive strength can only be taken at face value, at least from mechanics perspective. Nonetheless, the utmost importance of strain is expected since the stress-strain curve can be portioned into distinct regions such as the initial peak stress region, plateau, and densification regions according to the value of the strain.

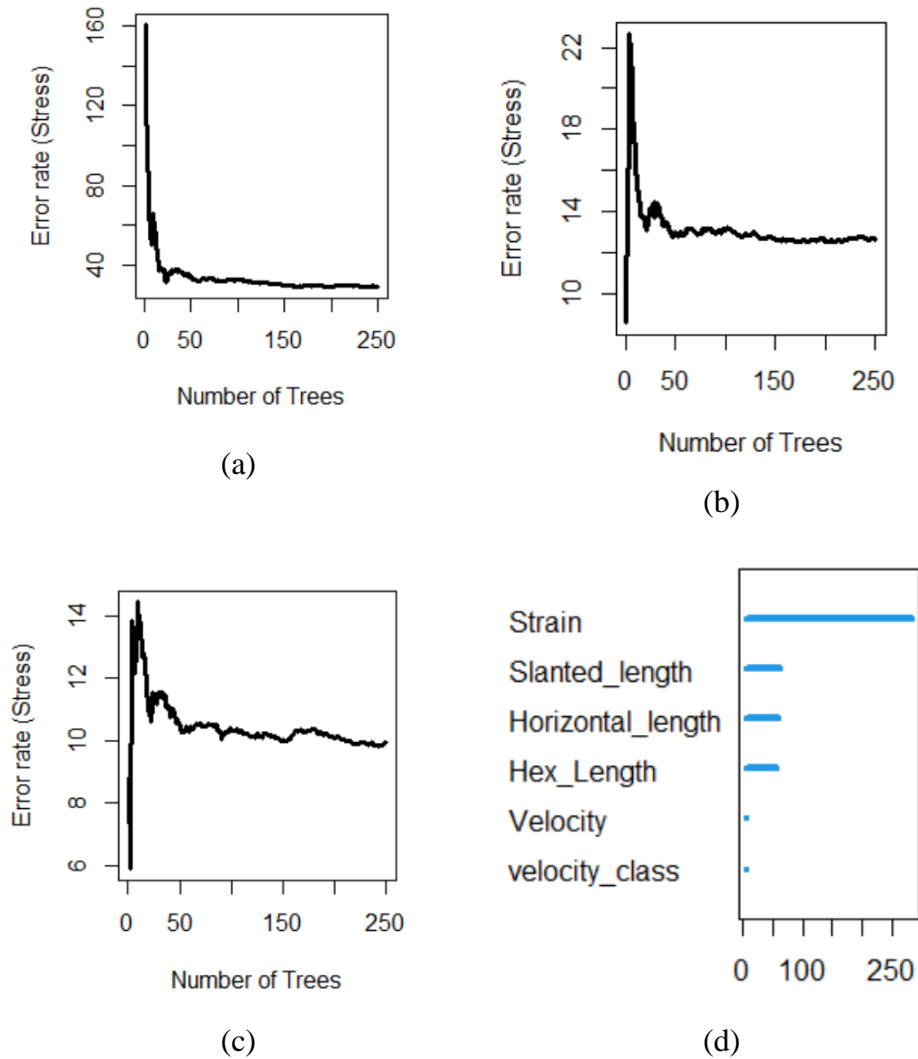


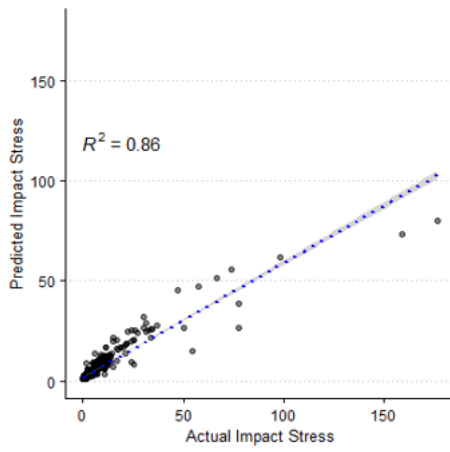
Figure 21: (a) OOB error vs the number of trees for *CR-RF1*; (b) OOB error vs the number of trees for *CR-RF2*; (c) OOB error vs the number of trees for *CR-RF3*; (d) variable importance plot for *CR-RF3*.

In addition to using the OOB error rate to assess the three RF models, Table 6 compares the models' performance in terms of other well-known performance metrics (R^2 , MAE and $RMSE$). Unlike the OOB which assesses the models' strength based on the training data, the results in Table 6 encompass the performance metrics concerning both training and test datasets. The table shows that the model with the 70:30 partition ratio (i.e., *CR-RF3*) again has a better performance across the three metrics. It exhibits an R^2 , MAE and $RMSE$ values of 96.6%, 0.375 and 2.27 MPa for the testing data. Figure 22 represents the goodness-of-fit plots that compare the actual stress values from the numerical experiment contained in the test dataset and the stress values predicted by the three RF models. As observed from the figure, the learned RF model is found to fits well with the actual stress distribution, reflecting good reliability in predicting the crushing stress response in the unseen data set.

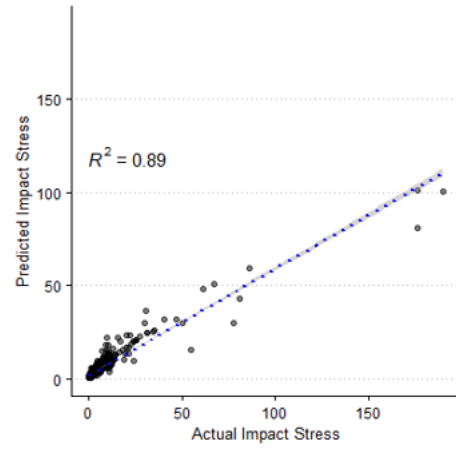
The performance of the *CR-RF3* is scrutinized further in Figure 23, which highlights the small prediction error is linked to the high-stress value. However, overall, the *CR-RF3* RF model shows an impressive performance across all classes of velocity values.

Table 6: Summary of performance metrics for the three RF models on the testing dataset

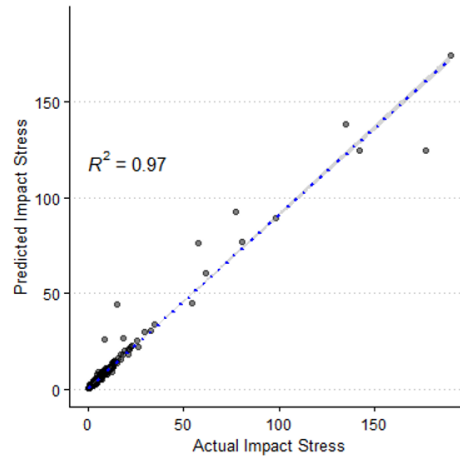
<i>RF Model</i>	<i>R</i> ²		<i>MAE</i>		<i>RMSE</i>	
	Training	Testing	Training	Testing	Training	Test
<i>CR-RF1</i>	0.919	0.856	1.230	1.140	4.700	4.460
<i>CR-RF2</i>	0.917	0.894	1.150	1.320	4.270	5.170
<i>CR-RF3</i>	0.986	0.966	0.279	0.375	1.190	2.270



(a) *CR-RF1*



(b) *CR-RF2*



(c) *CR-RF3*

Figure 22: R-squared plots of the numerical experiment stress (MPa) data against the predictions by the three RF models.

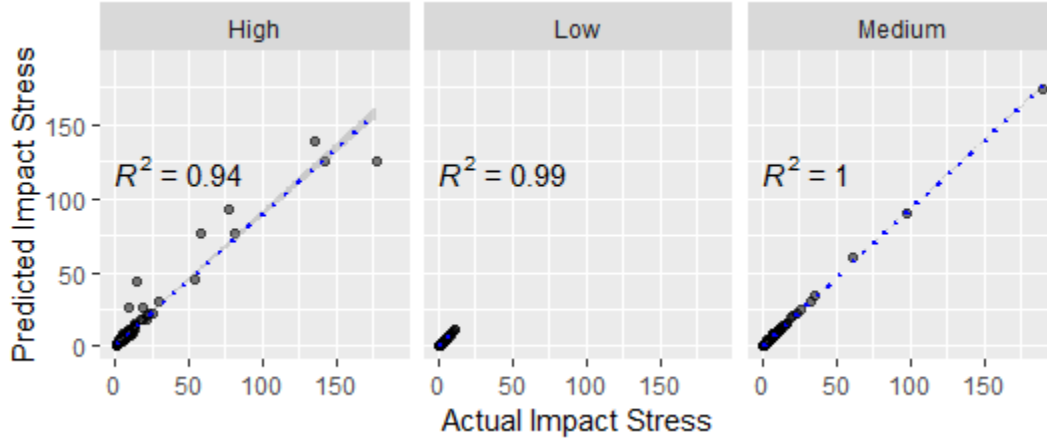


Figure 23: Breakdown of the R squared plots of the numerical experiment stress data against the predictions by the optimal RF model (*CR-RF3*)

Finally, the *CR-RF3* model was used to predict the stress-strain curve of the HHRH structure when $\gamma = 0.1$ at $V = 20 \text{ m/s}$. The result is shown in Figure 24. As reflected in the figure, the predicted stress-strain curve fits very well with the actual curve and hence, can capture the actual crashworthiness of the structure with great reliability. Put together, the strong performance of the RF model bodes well for its use in the detection of impact events or detection of collision impacts. With the help of embedded sensors, the instantaneous state of strain in intelligent auxetic structures can be acquired during an impact event. Feeding this information to a pre-trained RF model for automated prediction then presents a promising approach for condition monitoring of intelligent structures.

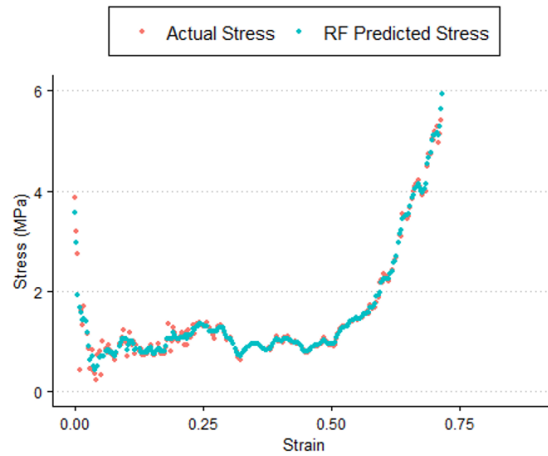


Figure 24: Predicting the stress-strain curve of the HHRH structure when $\gamma = 0.1$ at $V = 20 \text{ m/s}$

4. Conclusion and recommendation

A primary motivation for the presented work is to improve the stiffness of the conventional re-entrant auxetics, and hence its crashworthiness, without sacrificing the beneficial negative Poisson's ratio effect. Along this line, sections of this paper have discussed the performance of a proposed hybrid hierarchical re-entrant structures (HHRH) that involves reinforcing the regular re-entrant structure's vertexes with hexagonal mini-unit cells. Controlled by a scaling factor, the size of the hexagon element is varied to assess its influence on the impact response of the parent re-entrant auxetic structure. With the geometric model of the new structure accomplished, a numerical simulation of the nonlinear response under impact is established. The finite element (FE) simulation set-up was first validated with published studies and found to show excellent agreement. The nonlinear FE model was then employed to study the crushing response and crashworthiness of the HHRH at specific range of impacting velocities. Towards the development of intelligent auxetic structure, a random forest (RF) machine learning model was developed to learn the crushing stress of the different models given geometric and strain inputs. Overall, the following conclusions are noted. First, the proposed HHRH shows a complex deformation mode that integrates the behaviour of the reinforcing hexagonal elements and that of the parent re-entrant structure. Second, at intermediate and high impacting velocities, the HHRH exhibits lower peak stress than the conventional re-entrant auxetics. Moreover, due to the increased effective wall thickness, the HHRH requires a very high crushing force and experiences early densification. Importantly, the HHRH structures are found to maintain the auxetic behaviour and showed an enhanced negative Poisson's ratio effect compared to the regular re-entrant structure. Furthermore, an optimized RF model grown with 250 trees predicted the crushing stress of the testing data set with a coefficient of correlation that is as high as 97%, with an RMSE of around 2.27, showing promising potential for the development of intelligent auxetic structures.

Despite the findings highlighted above, further generalizability of this study is bound by some limitations. First, the simulations of the impact response were based on elastic-perfectly plastic material behaviour. While this material model provides reasonable accuracy for a certain class of materials under certain loading conditions, it neither allows for the simulation of hardening and softening effects nor does it account for rate-dependent behaviour that may accompany plasticity. Second, the development of the machine learning technique has been based on a limited range of impacting velocity along with a restrained axial crushing force. To enhance the generalization of the RF model, expanding the scope of the training data to include a wider range of impacting velocity and oblique impacting loads will be essential. These two limitations, among others, form part of the future work for this investigation.

Data Availability

The raw/processed data required to reproduce these findings cannot be shared at this time as the data also forms part of an ongoing study.

References

- [1] L. J. Gibson, and M. F. Ashby, *Cellular Solids: Structure and Properties*: Cambridge University Press, 1999.
- [2] L. J. Gibson, "Cellular solids," *Mrs Bulletin*, vol. 28, no. 4, pp. 270-274, 2003.
- [3] S. D. Papka, and S. Kyriakides, "In-plane compressive response and crushing of honeycomb," *Journal of the Mechanics and Physics of Solids*, vol. 42, no. 10, pp. 1499-1532, 1994/10/01/, 1994.
- [4] Q. Gao, L. Wang, Z. Zhou, Z. D. Ma, C. Wang, and Y. Wang, "Theoretical, numerical and experimental analysis of three-dimensional double-V honeycomb," *Materials & Design*, vol. 139, pp. 380-391, 2018/02/05/, 2018.
- [5] J. Zhang, G. Lu, and Z. You, "Large deformation and energy absorption of additively manufactured auxetic materials and structures: A review," *Composites Part B: Engineering*, vol. 201, pp. 108340, 2020/11/15/, 2020.
- [6] K. E. Evans, "The design of doubly curved sandwich panels with honeycomb cores," *Composite Structures*, vol. 17, no. 2, pp. 95-111, 1991/01/01/, 1991.
- [7] V. H. Carneiro, J. Meireles, and H. Puga, "Auxetic materials — A review," *Materials Science-Poland*, vol. 31, no. 4, pp. 561-571, 2013/10/01, 2013.
- [8] K. E. Evans, and A. Alderson, "Auxetic materials: functional materials and structures from lateral thinking!," *Advanced materials*, vol. 12, no. 9, pp. 617-628, 2000.
- [9] F. Scarpa, J. Giacomini, A. Bezazi, and W. Bullough, "Dynamic behavior and damping capacity of auxetic foam pads." p. 61690T.
- [10] F. Dos Reis, and J. F. Ganghoffer, "Equivalent mechanical properties of auxetic lattices from discrete homogenization," *Computational Materials Science*, vol. 51, no. 1, pp. 314-321, 2012/01/01/, 2012.
- [11] A. E. H. Love, *A treatise on the mathematical theory of elasticity*: Cambridge university press, 2013.
- [12] Y. Prawoto, "Seeing auxetic materials from the mechanics point of view: A structural review on the negative Poisson's ratio," *Computational Materials Science*, vol. 58, pp. 140-153, 2012/06/01/, 2012.
- [13] R. Lakes, "Negative Poisson's ratio materials [8]," *Science*, vol. 238, no. 4826, pp. 551, 1987.
- [14] R. Lakes, "Foam structures with a negative poisson's ratio," *Science*, vol. 235, no. 4792, pp. 1038-1040, 1987.
- [15] C. W. Smith, J. Grima, and K. Evans, "A novel mechanism for generating auxetic behaviour in reticulated foams: missing rib foam model," *Acta materialia*, vol. 48, no. 17, pp. 4349-4356, 2000.
- [16] G. Wei, "Negative and conventional Poisson's ratios of polymeric networks with special microstructures," *The Journal of chemical physics*, vol. 96, no. 4, pp. 3226-3233, 1992.
- [17] D. Yang, S. Lee, and F. Huang, "Geometric effects on micropolar elastic honeycomb structure with negative Poisson's ratio using the finite element method," *Finite elements in analysis and design*, vol. 39, no. 3, pp. 187-205, 2003.

- [18] F. Dos Reis, and J. Ganghoffer, "Equivalent mechanical properties of auxetic lattices from discrete homogenization," *Computational Materials Science*, vol. 51, no. 1, pp. 314-321, 2012.
- [19] S. Gonella, and M. Ruzzene, "Homogenization and equivalent in-plane properties of two-dimensional periodic lattices," *International Journal of Solids and Structures*, vol. 45, no. 10, pp. 2897-2915, 2008.
- [20] L. Rothenburg, A. A. Berlin, and R. J. Bathurst, "Microstructure of isotropic materials with negative Poisson's ratio," *Nature*, vol. 354, no. 6353, pp. 470-472, 1991.
- [21] C. Luo, C. Z. Han, X. Y. Zhang, X. G. Zhang, X. Ren, and Y. M. Xie, "Design, manufacturing and applications of auxetic tubular structures: A review," *Thin-Walled Structures*, vol. 163, pp. 107682, 2021.
- [22] Z. Wang, C. Luan, G. Liao, J. Liu, X. Yao, and J. Fu, "Progress in auxetic mechanical metamaterials: structures, characteristics, manufacturing methods, and applications," *Advanced Engineering Materials*, vol. 22, no. 10, pp. 2000312, 2020.
- [23] W. Wu, W. Hu, G. Qian, H. Liao, X. Xu, and F. Berto, "Mechanical design and multifunctional applications of chiral mechanical metamaterials: A review," *Materials & Design*, vol. 180, pp. 107950, 2019.
- [24] W. Yang, Z.-M. Li, W. Shi, B.-H. Xie, and M.-B. Yang, "Review on auxetic materials," *Journal of materials science*, vol. 39, no. 10, pp. 3269-3279, 2004.
- [25] H. M. Kolken, and A. Zadpoor, "Auxetic mechanical metamaterials," *RSC advances*, vol. 7, no. 9, pp. 5111-5129, 2017.
- [26] J. B. Choi, and R. S. Lakes, "Analysis of elastic modulus of conventional foams and of re-entrant foam materials with a negative Poisson's ratio," *International Journal of Mechanical Sciences*, vol. 37, no. 1, pp. 51-59, 1995/01/01/, 1995.
- [27] J. Lee, J. B. Choi, and K. Choi, "Application of homogenization FEM analysis to regular and re-entrant honeycomb structures," *Journal of Materials Science*, vol. 31, no. 15, pp. 4105-4110, 1996/08/01, 1996.
- [28] H. Wan, H. Ohtaki, S. Kotosaka, and G. Hu, "A study of negative Poisson's ratios in auxetic honeycombs based on a large deflection model," *European Journal of Mechanics-A/Solids*, vol. 23, no. 1, pp. 95-106, 2004.
- [29] M. S. Rad, Y. Prawoto, and Z. Ahmad, "Analytical solution and finite element approach to the 3D re-entrant structures of auxetic materials," *Mechanics of Materials*, vol. 74, pp. 76-87, 2014.
- [30] M. H. Fu, O. T. Xu, L. L. Hu, and T. X. Yu, "Nonlinear shear modulus of re-entrant hexagonal honeycombs under large deformation," *International Journal of Solids and Structures*, vol. 80, pp. 284-296, 2016/02/01/, 2016.
- [31] W. Liu, N. Wang, J. Huang, and H. Zhong, "The effect of irregularity, residual convex units and stresses on the effective mechanical properties of 2D auxetic cellular structure," *Materials Science and Engineering: A*, vol. 609, pp. 26-33, 2014/07/15/, 2014.
- [32] Q. Gao, Z. Ding, and W.-H. Liao, "Effective elastic properties of irregular auxetic structures," *Composite Structures*, vol. 287, pp. 115269, 2022/05/01/, 2022.

- [33] F. Scarpa, L. G. Ciffo, and J. R. Yates, "Dynamic properties of high structural integrity auxetic open cell foam," *Smart Materials and Structures*, vol. 13, no. 1, pp. 49-56, 2003/11/25, 2003.
- [34] F. Scarpa, J. R. Yates, L. G. Ciffo, and S. Patsias, "Dynamic crushing of auxetic open-cell polyurethane foam," *Proceedings of the Institution of Mechanical Engineers, Part C: Journal of Mechanical Engineering Science*, vol. 216, no. 12, pp. 1153-1156, 2002.
- [35] B. Henderson, J. P. M. Whitty, P. Myler, and C. Chirwa, "Crash performance of cellular foams with reduced relative density part 2: rib deletion," *International Journal of Crashworthiness*, vol. 12, no. 6, pp. 689-698, 2007/12/17, 2007.
- [36] X.-c. Zhang, H.-m. Ding, L.-q. An, and X.-l. Wang, "Numerical investigation on dynamic crushing behavior of auxetic honeycombs with various cell-wall angles," *Advances in Mechanical Engineering*, vol. 7, no. 2, pp. 679678, 2015.
- [37] L. L. Hu, M. Z. Zhou, and H. Deng, "Dynamic crushing response of auxetic honeycombs under large deformation: Theoretical analysis and numerical simulation," *Thin-Walled Structures*, vol. 131, pp. 373-384, 2018/10/01/, 2018.
- [38] Q. Gao, W.-H. Liao, and L. Wang, "On the low-velocity impact responses of auxetic double arrowed honeycomb," *Aerospace Science and Technology*, vol. 98, pp. 105698, 2020/03/01/, 2020.
- [39] X. Jin, Z. Wang, J. Ning, G. Xiao, E. Liu, and X. Shu, "Dynamic response of sandwich structures with graded auxetic honeycomb cores under blast loading," *Composites Part B: Engineering*, vol. 106, pp. 206-217, 2016/12/01/, 2016.
- [40] T. Fíla, P. Zlámál, O. Jiroušek, J. Falta, P. Koudelka, D. Kytýř, T. Doktor, and J. Valach, "Impact Testing of Polymer-filled Auxetics Using Split Hopkinson Pressure Bar," *Advanced Engineering Materials*, vol. 19, no. 10, pp. 1700076, 2017.
- [41] G. Imbalzano, S. Linforth, T. D. Ngo, P. V. S. Lee, and P. Tran, "Blast resistance of auxetic and honeycomb sandwich panels: Comparisons and parametric designs," *Composite Structures*, vol. 183, pp. 242-261, 2018/01/01/, 2018.
- [42] T.-C. Lim, *Mechanics of metamaterials with negative parameters*: Springer Nature, 2020.
- [43] K. K. Saxena, R. Das, and E. P. Calius, "Three decades of auxetics research— materials with negative Poisson's ratio: a review," *Advanced Engineering Materials*, vol. 18, no. 11, pp. 1847-1870, 2016.
- [44] D. Li, J. Yin, L. Dong, and R. S. Lakes, "Strong re-entrant cellular structures with negative Poisson's ratio," *Journal of materials science*, vol. 53, no. 5, pp. 3493-3499, 2018.
- [45] Q. Gao, L. Wang, Y. Wang, and C. Wang, "Crushing analysis and multiobjective crashworthiness optimization of foam-filled ellipse tubes under oblique impact loading," *Thin-Walled Structures*, vol. 100, pp. 105-112, 2016/03/01/, 2016.
- [46] W. Liu, N. Wang, T. Luo, and Z. Lin, "In-plane dynamic crushing of re-entrant auxetic cellular structure," *Materials & Design*, vol. 100, pp. 84-91, 2016/06/15/, 2016.
- [47] T. Baran, and M. Öztürk, "In-plane elasticity of a strengthened re-entrant honeycomb cell," *European Journal of Mechanics - A/Solids*, vol. 83, pp. 104037, 2020/09/01/, 2020.
- [48] K. Zied, M. Osman, and T. Elmahdy, "Enhancement of the in-plane stiffness of the hexagonal re-entrant auxetic honeycomb cores," *physica status solidi (b)*, vol. 252, no. 12, pp. 2685-2692, 2015.

- [49] A. Ingrole, A. Hao, and R. Liang, "Design and modeling of auxetic and hybrid honeycomb structures for in-plane property enhancement," *Materials & Design*, vol. 117, pp. 72-83, 2017/03/05/, 2017.
- [50] N. Novak, M. Borovinšek, M. Vesenjāk, M. Wormser, C. Körner, S. Tanaka, K. Hokamoto, and Z. Ren, "Crushing behavior of graded auxetic structures built from inverted tetrapods under impact," *physica status solidi (b)*, vol. 256, no. 1, pp. 1800040, 2019.
- [51] Q. Gao, and W.-H. Liao, "Energy absorption of thin walled tube filled with gradient auxetic structures-theory and simulation," *International Journal of Mechanical Sciences*, vol. 201, pp. 106475, 2021/07/01/, 2021.
- [52] X. Wu, Y. Su, and J. Shi, "In-plane impact resistance enhancement with a graded cell-wall angle design for auxetic metamaterials," *Composite Structures*, vol. 247, pp. 112451, 2020/09/01/, 2020.
- [53] X. Li, Q. Wang, Z. Yang, and Z. Lu, "Novel auxetic structures with enhanced mechanical properties," *Extreme Mechanics Letters*, vol. 27, pp. 59-65, 2019/02/01/, 2019.
- [54] L.-q. An, X.-c. Zhang, H.-x. Wu, and W.-q. Jiang, "In-plane dynamic crushing and energy absorption capacity of self-similar hierarchical honeycombs," *Advances in Mechanical Engineering*, vol. 9, no. 6, pp. 1687814017703896, 2017.
- [55] W. Zhang, S. Zhao, R. Sun, F. Scarpa, and J. Wang, "In-plane mechanical behavior of a new star-re-entrant hierarchical metamaterial," *Polymers*, vol. 11, no. 7, pp. 1132, 2019.
- [56] H. L. Tan, Z. C. He, K. X. Li, E. Li, A. G. Cheng, and B. Xu, "In-plane crashworthiness of re-entrant hierarchical honeycombs with negative Poisson's ratio," *Composite Structures*, vol. 229, pp. 111415, 2019/12/01/, 2019.
- [57] J. Hou, D. Li, and L. Dong, "Mechanical behaviors of hierarchical cellular structures with negative Poisson's ratio," *Journal of Materials Science*, vol. 53, no. 14, pp. 10209-10216, 2018.
- [58] M. Ghajari, Z. Sharif-Khodaei, M. H. Aliabadi, and A. Apicella, "Identification of impact force for smart composite stiffened panels," *Smart Materials and Structures*, vol. 22, no. 8, pp. 085014, 2013/07/11, 2013.
- [59] F. Akhavan, S. E. Watkins, and K. Chandrashekhara, "Recovery of impact contact forces of composite plates using fiber optic sensors and neural networks." pp. 277-288.
- [60] K. Chandrashekhara, A. C. Okafor, and Y. Jiang, "Estimation of contact force on composite plates using impact-induced strain and neural networks," *Composites Part B: Engineering*, vol. 29, no. 4, pp. 363-370, 1998.
- [61] Z. Li, Q. Gao, S. Yang, L. Wang, and J. Tang, "Comparative study of the in-plane uniaxial and biaxial crushing of hexagonal, re-entrant, and mixed honeycombs," *Journal of Sandwich Structures & Materials*, vol. 21, no. 6, pp. 1991-2013, 2019.
- [62] L. Wei, X. Zhao, Q. Yu, and G. Zhu, "A novel star auxetic honeycomb with enhanced in-plane crushing strength," *Thin-Walled Structures*, vol. 149, pp. 106623, 2020/04/01/, 2020.
- [63] A. Alomarah, D. Ruan, and S. Masood, "Tensile properties of an auxetic structure with re-entrant and chiral features—a finite element study," *The International Journal of Advanced Manufacturing Technology*, vol. 99, no. 9, pp. 2425-2440, 2018/12/01, 2018.
- [64] D. L. Logan, *A first course in the finite element method*: Cengage Learning, 2016.

- [65] L. Breiman, "Random Forests," *Machine Learning*, vol. 45, no. 1, pp. 5-32, 2001/10/01, 2001.
- [66] M. Pal, "Random forest classifier for remote sensing classification," *International journal of remote sensing*, vol. 26, no. 1, pp. 217-222, 2005.
- [67] Y. Qi, "Random forest for bioinformatics," *Ensemble machine learning*, pp. 307-323: Springer, 2012.
- [68] S. O. Olatunji, S. Alotaibi, E. Almutairi, Z. Alrabae, Y. Almajid, R. Altabee, M. Altassan, M. I. B. Ahmed, M. Farooqui, and J. Alhiyafi, "Early diagnosis of thyroid cancer diseases using computational intelligence techniques: A case study of a Saudi Arabian dataset," *Computers in Biology and Medicine*, vol. 131, pp. 104267, 2021.
- [69] D. K. Lim, K. Mustapha, and C. Pagwiwoko, "Delamination detection in composite plates using random forests," *Composite Structures*, vol. 278, pp. 114676, 2021.
- [70] A. Liaw, and M. Wiener, "Classification and regression by randomForest," *R news*, vol. 2, no. 3, pp. 18-22, 2002.
- [71] R. C. Team, "R: A Language and Environment for Statistical Computing," R Foundation for Statistical Computing, 2020.
- [72] G. Biau, and E. Scornet, "A random forest guided tour," *Test*, vol. 25, no. 2, pp. 197-227, 2016.
- [73] G. James, D. Witten, T. Hastie, and R. Tibshirani, *An Introduction to Statistical Learning: with Applications in R*: Springer New York, 2013.
- [74] K. J. Archer, and R. V. Kimes, "Empirical characterization of random forest variable importance measures," *Computational statistics & data analysis*, vol. 52, no. 4, pp. 2249-2260, 2008.
- [75] P. Probst, M. N. Wright, and A. L. Boulesteix, "Hyperparameters and tuning strategies for random forest," *Wiley Interdisciplinary Reviews: Data Mining and Knowledge Discovery*, vol. 9, no. 3, pp. e1301, 2019.
- [76] T. Hastie, R. Tibshirani, and J. Friedman, *The elements of statistical learning: data mining, inference, and prediction*: Springer Science & Business Media, 2009.
- [77] Y. J. Wong, S. K. Arumugasamy, and K. Mustapha, "Development of a computational predictive model for the nonlinear in-plane compressive response of sandwich panels with bio-foam," *Composite Structures*, vol. 212, pp. 423-433, 2019.
- [78] Y. J. Wong, K. B. Mustapha, Y. Shimizu, A. Kamiya, and S. K. Arumugasamy, "Development of surrogate predictive models for the nonlinear elasto-plastic response of medium density fibreboard-based sandwich structures," *International Journal of Lightweight Materials and Manufacture*, vol. 4, no. 3, pp. 302-314, 2021/09/01/, 2021.
- [79] X. Hou, Z. Deng, and K. Zhang, "Dynamic crushing strength analysis of auxetic honeycombs," *Acta Mechanica Solida Sinica*, vol. 29, no. 5, pp. 490-501, 2016.
- [80] H. Wang, Z. Lu, Z. Yang, and X. Li, "A novel re-entrant auxetic honeycomb with enhanced in-plane impact resistance," *Composite Structures*, vol. 208, pp. 758-770, 2019/01/15/, 2019.
- [81] X. Zhao, Q. Gao, L. Wang, Q. Yu, and Z. Ma, "Dynamic crushing of double-arrowed auxetic structure under impact loading," *Materials & Design*, vol. 160, pp. 527-537, 2018.

- [82] S. Mohsenizadeh, R. Alipour, M. Shokri Rad, A. Farokhi Nejad, and Z. Ahmad, "Crashworthiness assessment of auxetic foam-filled tube under quasi-static axial loading," *Materials & Design*, vol. 88, pp. 258-268, 2015/12/25/, 2015.
- [83] K. P. Logakannan, V. Ramachandran, J. Rengaswamy, and D. Ruan, "Dynamic Performance of a 3D Re-entrant Structure," *Mechanics of Materials*, vol. 148, pp. 103503, 2020/09/01/, 2020.
- [84] M. Kuhn, "Building predictive models in R using the caret package," *Journal of statistical software*, vol. 28, no. 1, pp. 1-26, 2008.
- [85] X. Chen, and H. Ishwaran, "Random forests for genomic data analysis," *Genomics*, vol. 99, no. 6, pp. 323-329, 2012/06/01/, 2012.
- [86] H. Ishwaran, "Variable importance in binary regression trees and forests," *Electronic Journal of Statistics*, vol. 1, pp. 519-537, 2007.